NeuroImage 256 (2022) 119219

Contents lists available at ScienceDirect

NeuroImage

journal homepage: www.elsevier.com/locate/neuroimage

Improved diffusion parameter estimation by incorporating T_2 relaxation properties into the DKI-FWE model

Vincenzo Anania[a,b,*], Quinten Collier[a], Jelle Veraart[a,c], Annemieke E. Buikema[a], Floris Vanhevel[d], Thibo Billiet[b], Ben Jeurissen[a,e], Arnold J. den Dekker[a,e], Jan Sijbers[a,e]

[a] *imec-Vision Lab, Department of Physics, University of Antwerp, Antwerp, Belgium*
[b] *ico**metrix**, Leuven, Belgium*
[c] *Bernard and Irene Schwartz Center for Biomedical Imaging, Department of Radiology, New York University Grossman School of Medicine, New York, NY, USA*
[d] *Department of Radiology, University of Antwerp, Antwerp University Hospital, Belgium*
[e] *μNEURO Research Centre of Excellence, University of Antwerp, Antwerp, Belgium*

ARTICLE INFO

Keywords:
Diffusion MRI
Partial volume effects
Free water elimination
Kurtosis
DKI
T_2 relaxation

ABSTRACT

The free water elimination (FWE) model and its kurtosis variant (DKI-FWE) can separate tissue and free water signal contributions, thus providing tissue-specific diffusional information. However, a downside of these models is that the associated parameter estimation problem is ill-conditioned, necessitating the use of advanced estimation techniques that can potentially bias the parameter estimates. In this work, we propose the T_2-DKI-FWE model that exploits the T_2 relaxation properties of both compartments, thereby better conditioning the parameter estimation problem and providing, at the same time, an additional potential biomarker (the T_2 of tissue). In our approach, the T_2 of tissue is estimated as an unknown parameter, whereas the T_2 of free water is assumed known a priori and fixed to a literature value (1573 ms). First, the error propagation of an erroneous assumption on the T_2 of free water is studied. Next, the improved conditioning of T_2-DKI-FWE compared to DKI-FWE is illustrated using the Cramér-Rao lower bound matrix. Finally, the performance of the T_2-DKI-FWE model is compared to that of the DKI-FWE and T_2-DKI models on both simulated and real datasets. The error due to a biased approximation of the T_2 of free water was found to be relatively small in various diffusion metrics and for a broad range of erroneous assumptions on its underlying ground truth value. Compared to DKI-FWE, using the T_2-DKI-FWE model is beneficial for the identifiability of the model parameters. Our results suggest that the T_2-DKI-FWE model can achieve precise and accurate diffusion parameter estimates, through effective reduction of free water partial volume effects and by using a standard nonlinear least squares approach. In conclusion, incorporating T_2 relaxation properties into the DKI-FWE model improves the conditioning of the model fitting, while only requiring an acquisition scheme with at least two different echo times.

1. Introduction

Diffusion-weighted magnetic resonance imaging (DW-MRI) is a non-invasive imaging modality with a unique sensitivity to the directional displacement of water molecules (Stejskal and Tanner, 1965). Within typical experimental diffusion times of 30 to 50 ms, the mean displacement of water molecules in living tissue is expected to be in the order of a few tens of microns, allowing DW-MRI to probe the cellular microstructure of tissue in vivo, for example in the brain. To compensate for the intrinsically low signal-to-noise ratio (SNR) of diffusion MRI (dMRI) data, one is typically bound to limited spatial resolutions making the image voxels relatively large (2^3 to 3^3 mm^3) and thus susceptible to partial volume effects (PVEs). Consequently, the interpretation of diffusion metrics in voxels containing different tissue types may become ambiguous. A notorious example of a partial volume effect is the presence of free-diffusing fluid such as cerebrospinal fluid (CSF) contamination or edema (Metzler-Baddeley et al., 2012). Inside the CSF or edema, water molecules can move freely, resulting in apparent diffusion coefficients (ADC) that widely exceed the ADC measurements in normal white matter (WM) brain tissue. Diffusion metrics in the voxels affected by partial volumes will represent a weighted average of tissue and free water and may therefore lose their reliability as biomarkers for tissue-specific changes. For this reason, correcting for PVEs in dMRI data is of paramount importance for the characterization of tissue microstructure with reduced confounding effects in both healthy and pathological conditions. To tackle this problem, we present a novel approach that is

* Corresponding author at: imec-Vision Lab, Department of Physics, University of Antwerp, Antwerp, Belgium.
E-mail address: vincenzo.anania@uantwerpen.be (V. Anania).

https://doi.org/10.1016/j.neuroimage.2022.119219.
Received 24 September 2021; Received in revised form 8 April 2022; Accepted 14 April 2022
Available online 18 April 2022.

based on 1) combined diffusion kurtosis (DKI) and T_2-weighted imaging acquisitions and 2) a two-compartment model, which separates the signal contributions from tissue and free water. Our approach allows us to extract partial volume-robust diffusion metrics and, at the same time, creates a better-conditioned parameter estimation problem compared to T_2-independent techniques.

Pierpaoli and Jones (2004) were the first to propose a two-compartment diffusion model for partial volume correction in diffusion-weighted imaging. Pasternak et al. (2009) expanded on this work and introduced the free water elimination (FWE) model, which represents the diffusion-weighted MR signal, S_{FWE}, as:

$$S_{\mathrm{FWE}} = (1-f)S_{\mathrm{tissue}} + fS_{\mathrm{csf}}. \tag{1}$$

In (Pasternak et al., 2009), the signal contribution of the tissue, S_{tissue}, is modeled using the diffusion tensor imaging (DTI) model (Basser et al., 1994; Le Bihan et al., 2001), thus we will refer to this model as DTI-FWE. The parameter f defines the fraction of the diffusion signal that corresponds to the free water compartment, also known as the free water fraction, and S_{csf} denotes the signal contribution of the free water compartment. To date, FWE is still the most used diffusion model to eliminate free water-like signal contributions. When fitting the two-compartment DTI-FWE model to dMRI data, the fitting problem is ill-conditioned for conventional single-shell acquisitions (Pasternak et al., 2009). Therefore, standard estimation techniques like nonlinear least squares (NLS) may easily converge to local minima due to a flat optimization landscape. To stabilize the fitting problem for single-shell acquisitions, still prevalent in clinical practice due to acquisition time constraints, careful parameter initialization and spatially regularized gradient descent algorithms can be used (Ismail et al., 2018; Parker et al., 2020; Pasternak et al., 2014, 2009). Although these approaches may provide plausible estimates, it has been recently pointed out that free water DTI estimates from single b-valued diffusion data need to be interpreted with care (Golub et al., 2021).

However, using multi-shell (at least two non-zero b-values) data can provide an initialization of the parameter estimates much closer to the actual minima leading to more reliable DTI-FWE estimates that can be obtained using linear and nonlinear least squares approaches in combination (Bergmann et al., 2020; Hoy et al., 2014). Recently, the FWE model was adapted by describing S_{tissue} with the DKI model (Jensen et al., 2005), resulting in the DKI-FWE model (Collier et al., 2018). DTI parametrizes the Gaussian component of the displacement probability density function (PDF) of water molecules, whereas DKI includes additional parameters that quantify non-Gaussian diffusivity. In most tissues, heterogeneity and biological restrictions, such as cell membranes and myelin sheets, cause the distribution of the water diffusion to be non-Gaussian, hence DKI is considered to be a more accurate representation of the DW-MR signal compared to DTI (Jensen and Helpern, 2010; Jensen et al., 2005).

Like DTI-FWE, the main limiting property of the bi-exponential DKI-FWE model is represented by the ill-conditioned inverse problem of estimating the model parameters from measured DW data. For DKI-FWE, the ill-conditionedness of the fitting problem was addressed by using statistical priors (Collier et al., 2018). Although statistical priors allow for a more stable model fitting procedure, they also impose certain assumptions on the parameter values that may bias the results. Another pitfall of the aforementioned bi-exponential models is that they fail to account for large differences in T_2 relaxation time of tissue, $T_2^{\mathrm{tissue}} \approx 70-100$ ms (Stanisz et al., 2005; Whittall et al., 1997), and CSF or edema, $T_2^{\mathrm{csf}} \approx 500-2100$ ms (Piechnik et al., 2009; Qin, 2011). The advantages of specifically accounting for T_2 in the two-compartment diffusion model consist in a better conditioning of the model fitting problem (Collier et al., 2017) and a reduced bias in DTI metrics caused by PVEs (Farrher et al., 2018). Moreover, the T_2 weighting term, if explicitly modeled, will no longer be incorporated in the parameter f thus making f a non-T_2-weighted free water fraction. Since $T_2^{\mathrm{csf}} >> T_2^{\mathrm{tissue}}$, the parameter f in the T_2-dependent model will be substantially smaller than the f in a T_2-independent model, like DTI-FWE or DKI-FWE.

Farrher et al. (2020) recently showed the potential of explicitly modeling the differences in the transverse relaxation times between tissue and CSF using two dedicated anisotropic diffusion fiber phantoms. In their study, the first phantom was designed to mimic PVEs that occur at the CSF-tissue interface, while the second phantom was intended to mimic the scenario of intra-tissue free water contamination. The authors pointed out that not accounting for the two separate compartments (CSF and tissue) may significantly alter the quantification of diffusion and relaxation properties in voxels affected by PVEs. Furthermore, the authors showed that the free water fraction can be overestimated when the model does not account for the echo time (TE) dependency of the signal decay. In the current work, we propose to incorporate the T_2 relaxation terms into the DKI-FWE model. By exploiting the TE dependency of the dMRI signal, the diffusion-related parameters can be estimated more precisely (Veraart et al., 2018), thereby also eliminating the need for advanced parameter estimation techniques to stabilize the fit. Moreover, combining diffusion and relaxation is also in line with recent trends in the MR community towards multidimensional MRI methods (Cheng et al., 2017; Fischi-Gomez et al., 2021; Jerome et al., 2016; Kim et al., 2017; Lampinen et al., 2020; Slator et al., 2021; Tax et al., 2021; Topgaard, 2017; Wang et al., 2014). In the context of multi-modal MRI, the advantages of the presented technique are its dependence on routinely used optimization approaches and the improved tissue specificity in the interpretation of diffusion metrics.

2. Methods

2.1. T_2-weighted diffusion kurtosis imaging free water elimination model

In this work, we extend the well-known two-compartment magnetic resonance diffusion model that separates the signal contributions of the tissue, S_{tissue}, and free water, S_{fw}, by including the compartment-specific T_2 relaxation times of tissue, T_2^{tissue}, and free water, T_2^{fw}, as:

$$\begin{aligned} &S(b, \boldsymbol{g}, \mathrm{TE}; \boldsymbol{\theta}_{\mathrm{tissue}}, f, d, T_2^{\mathrm{tissue}}, T_2^{\mathrm{fw}}) \\ &= S_{00}\left((1-f)\exp\left(-\mathrm{TE}/T_2^{\mathrm{tissue}}\right)S_{\mathrm{tissue}}(b, \boldsymbol{g}; \boldsymbol{\theta}_{\mathrm{tissue}}) + f\exp\left(-\mathrm{TE}/T_2^{\mathrm{fw}}\right)S_{\mathrm{fw}}(b; d)\right). \end{aligned} \tag{2}$$

Here, b and $\boldsymbol{g}$ denote the diffusion weighting strength and direction, respectively. S_{00} and d represent the non-diffusion-weighted signal ($b = 0$ ms/μm^2) at TE = 0 ms and the isotropic diffusivity of free water at body temperature, respectively, while $\boldsymbol{\theta}_{\mathrm{tissue}}$ denotes the parameter vector that characterizes the diffusion model used to represent the signal contribution of the tissue compartment. Using the Einstein-Smoluchowski relation (Einstein, 1905), which relates the diffusivity of a medium to its temperature, it is possible to analytically determine d to be approximately equal to 3 μm^2/ms at body temperature. The free water signal contribution is thus modeled as:

$$S_{\mathrm{fw}}(b) = \exp(-bd), \tag{3}$$

while we choose to represent S_{tissue} with the DKI model:

$$\begin{aligned} S_{\mathrm{tissue}} &= S_{\mathrm{DKI}}\left(b, \boldsymbol{g}; \boldsymbol{\theta}_{\mathrm{DKI}}\right) \\ &= \exp\left(-b\sum_{i,j=1}^{3} g_i g_j D_{ij} + \frac{b^2}{6}\left(\sum_{i=1}^{3}\frac{D_{ii}}{3}\right)^2 \sum_{i,j,k,l=1}^{3} g_i g_j g_k g_l W_{ijkl} + \mathcal{O}(b^3)\right) \\ &= \exp\left(-b\sum_{i,j=1}^{3} g_i g_j D_{ij} + \frac{b^2}{6}\sum_{i,j,k,l=1}^{3} g_i g_j g_k g_l K_{ijkl} + \mathcal{O}(b^3)\right). \end{aligned} \tag{4}$$

Here, D_{ij} represents the ij^{th} element of the fully symmetric second-order diffusion tensor $\boldsymbol{D}$, which can be characterized by 6 independent elements: $\boldsymbol{\theta}_D = \{D_{ij}\}_{i\le j\le 3}$. Furthermore, W_{ijkl} represents the $ijkl^{\mathrm{th}}$ element of the fully symmetric fourth-order diffusion kurtosis tensor $\boldsymbol{W}$, which can be characterized by 15 independent elements: $\boldsymbol{\theta}_W = \{W_{ijkl}\}_{i\le j\le k\le l\le 3}$. Our parametrization of the DKI model makes use of the scaled apparent kurtosis tensor $\boldsymbol{K} = \left(\sum_{i=1}^{3}\frac{D_{ii}}{3}\right)^2\boldsymbol{W} = \mathrm{MD}^2\boldsymbol{W}$ with

MD the mean diffusivity. In summary, the DKI model is parameterized by 21 independent parameters: $\theta_{\mathrm{DKI}} = [\theta_D, \theta_K = \mathrm{MD}^2\theta_W]$. We will refer to the combined model (2), where DKI models the tissue diffusion-weighted MR signal, as the "T_2-weighted diffusion kurtosis imaging free water elimination model", or T_2-DKI-FWE for short.

In simulation experiments, the performance of T_2-DKI-FWE will be compared in terms of accuracy and precision to that of the T_2-DKI model and the DKI-FWE model. Comparison to T_2-DKI is made to study the impact on the model parameters of accounting for PVEs by explicitly modeling a free water compartment. Comparing T_2-DKI-FWE to DKI-FWE will highlight the effect of accounting for the different T_2 of tissue and free water on the parameter estimation results. T_2-DKI models the T_2 and diffusion-weighted signal as:

$$S_{T_2-\mathrm{DKI}}(b, \boldsymbol{g}, \mathrm{TE}; \boldsymbol{\theta}_{\mathrm{DKI}}, T_2) = S_{00} \exp\left(-\mathrm{TE}/T_2\right) S_{\mathrm{DKI}}(b, \boldsymbol{g}; \boldsymbol{\theta}_{\mathrm{DKI}}), \tag{5}$$

while the TE-independent, diffusion-weighted MR signal modeled by DKI-FWE, can be written as:

$$S_{\mathrm{DKI-FWE}}(b, \boldsymbol{g}; \boldsymbol{\theta}_{\mathrm{DKI}}, f, d) = S_0\left((1-f)\, S_{\mathrm{DKI}}(b, \boldsymbol{g}; \boldsymbol{\theta}_{\mathrm{DKI}}) + f\, S_{\mathrm{fw}}(b; d)\right). \tag{6}$$

2.2. Data acquisition and pre-processing

For the real data experiments, a DW-MRI dataset of one healthy male volunteer (age: 29 years old) was acquired using a 3 T Siemens MAGNETOM PrismaFit system equipped with a 32-channel head coil and informed consent was obtained from the participant. During the acquisition, three consecutive repetitions were performed with different TEs: in particular, the first two repetitions were acquired with TE = 67 ms and the third one with TE = 120 ms. For the acquisition at TE = 67 ms, the diffusion time Δ (time interval between diffusion gradients) was 33.4 ms and the pulse duration δ was 16 ms, while at TE = 120 ms, Δ was 59.9 ms and δ 42.5 ms. All other settings were kept constant across repetitions.

The datasets were acquired using an EPI/spin-echo (SE) diffusion-weighted pulse sequence with an 88×88 acquisition matrix, from which an image was reconstructed with an isotropic voxel size of 2.5 mm, 58 slices and pulse repetition time (TR) of 4300 ms. The diffusion-weighted gradient settings consisted, for each repetition, of six $b = 0$ ms/μm^2 images and three b-value shells (b = 0.5, 1 and 2 ms/μm^2) with 30 non-collinear magnetic field gradient directions for each of the non-zero b-value shells. In agreement with (Collier et al., 2018), we adopted a protocol with four shells (including the $b = 0$ images) to avoid an ill-conditioned optimization problem. The maximum b-value, i.e., 2 ms/μm^2, was selected to ensure a balanced trade-off between the accuracy and the precision of the DKI model parameters (Chuhutin et al., 2017). The range of available TEs for the selected b-value range was 63–121 ms and, to set up a practical acquisition, we acquired diffusion-weighted volumes at two different TEs: one in the lower part of the range (67 ms) and one in the upper part (120 ms). The gradient directions were generated using electrostatic repulsion resulting in a set of 30 directions for each shell (Jones et al., 1999; Papadakis et al., 2000). GRAPPA with an acceleration factor 2 and adaptive combine reconstruction with a spatial matched filter (SMF) approach were used to accelerate the acquisition. The acquisition time was 7:08 min for each TE = 67 ms repetition and 7:14 min for the TE = 120 ms repetition.

After the acquisition, the following pre-processing steps were performed: first, the repetitions acquired with different TEs were concatenated in a single 4D image; next, the dMRI dataset was denoised by exploiting its inherent redundancy using random matrix theory (Veraart et al., 2016) and corrected for Gibbs ringing as described in (Kellner et al., 2016). Finally, the data were corrected for motion and eddy current induced distortions using in-house model-based motion correction software (Bai and Alexander, 2008).

In vivo data used in this paper will be available via a formal request to the corresponding author and a data sharing agreement should be signed by both parties. Pre-processing was performed using functions made available in the MRtrix3 software framework (Tournier et al., 2019).

2.3. Estimation of the model parameters

When solving ill-conditioned problems, the use of regularization or statistical priors can, on the one hand, help stabilize the model fit. On the other hand, it can also bias the results when the considered assumptions do not entirely hold. Consequently, in this work, all model parameters are estimated using a standard NLS approach, without regularization. The NLS model fits are performed in MATLAB (MATLAB, 2020) using the *fmincon* function with the interior point algorithm (Byrd et al., 2000; 1999; Waltz et al., 2006). The objective function of the NLS estimator can be formulated as:

$$\epsilon_{\mathrm{NLS}}(\boldsymbol{\theta}) = \frac{1}{2} \sum_{j=1}^{N_{\mathrm{DWI}}} (\widetilde{S}_j - S_j(\boldsymbol{\theta}))^2, \tag{7}$$

where the index j iterates over the signal acquisition directions N_{DWI}, $\widetilde{S}_j$ is the measured signal and S_j represents the signal predicted from the model, and thus expressed as a function of the model parameter vector $\boldsymbol{\theta}$. The size of $\boldsymbol{\theta}$ depends on the model chosen to represent the data: $\boldsymbol{\theta}_{T_2-\mathrm{DKI-FWE}} = [S_{00}, \boldsymbol{\theta}_D, \boldsymbol{\theta}_K, f, T_2^{\mathrm{tissue}}]$ is an array of 24 unknown parameters, while $\boldsymbol{\theta}_{T_2-\mathrm{DKI}} = [S_{00}, \boldsymbol{\theta}_D, \boldsymbol{\theta}_K, T_2]$ and $\boldsymbol{\theta}_{\mathrm{DKI-FWE}} = [S_0, \boldsymbol{\theta}_D, \boldsymbol{\theta}_K, f]$ contain 23 independent elements. When the T_2-DKI-FWE model is chosen to fit the observed data, estimating the value of the parameter T_2^{fw} simultaneously with the other model parameters runs the risk of being unstable, leading to T_2^{fw} estimates that are found near the posed constraints, thereby biasing f (Collier et al., 2017). Alternatively, one could estimate the value of T_2^{fw} in a CSF region beforehand. This would, however, require additional $b = 0$ images with a large TE range to reliably estimate the large T_2^{fw} value. Consequently, we propose to consider the value of T_2^{fw} as a constant which is determined from the literature: $T_2^{\mathrm{fw}} = 1573$ ms (Qin, 2011). The impact of setting a constant value for T_2^{fw} has been assessed in simulation experiments. To provide a physically plausible solution for the diffusion and kurtosis tensors ($\boldsymbol{D}$ and $\boldsymbol{W}$), the following constraints were posed (Tabesh et al., 2011; Veraart et al., 2011):

1. The apparent diffusion coefficient D_{APP} should be positive along each possible gradient direction:

$$D_{\mathrm{APP}}(\boldsymbol{g}) = \sum_{i,j=1}^{3} g_i g_j D_{ij} > 0. \tag{8}$$

2. The apparent kurtosis coefficient K_{APP} is assumed to be positive definite, thus this constraint provides a lower bound on K_{APP}:

$$K_{\mathrm{APP}}(\boldsymbol{g}) = \frac{\mathrm{MD}^2}{D_{\mathrm{APP}}(\boldsymbol{g})^2} \sum_{i,j,k,l=1}^{3} g_i g_j g_k g_l W_{ijkl} > 0. \tag{9a}$$

Considering that MD^2 and $D_{\mathrm{APP}}(\boldsymbol{g})^2$ are always positive, the expression (9a) can be simplified as

$$\sum_{i,j,k,l=1}^{3} g_i g_j g_k g_l W_{ijkl} > 0, \tag{9b}$$

or

$$\sum_{i,j,k,l=1}^{3} g_i g_j g_k g_l K_{ijkl} > 0, \tag{9c}$$

where $K_{ijkl} = \mathrm{MD}^2 W_{ijkl}$.

3. The third constraint poses an upper bound on K_{APP} to ensure that the log-transformed diffusion-weighted signal monotonically decreases as a function of the b-value:

$$K_{\mathrm{APP}}(\boldsymbol{g}) D_{\mathrm{APP}}(\boldsymbol{g})^2 - \frac{3 D_{\mathrm{APP}}(\boldsymbol{g})}{b_{\max}} \leq 0, \tag{10}$$

with $b_{\max}$ the maximum b-value selected in the acquisition settings.

Table 1
Lower bounds (lb), upper bounds (ub) and initialization values (init. val.) used for the NLS estimates of all the non-DKI model parameters.

Model parameter	lb	ub	init. val.
S_{00} (T_2-DKI, T_2-DKI-FWE)	0	inf	$\hat{S}_0$
S_0 (DKI-FWE)	0	inf	$\hat{S}_0$
f (DKI-FWE, T_2-DKI-FWE)	0	1	[0, 0.25, 0.5, 0.75]
T_2^{tissue} (T_2-DKI-FWE) [ms]	5	200	75
T_2 (T_2-DKI) [ms]	5	2500	75

The constraints on the apparent diffusion and kurtosis coefficients can be implemented in the form of linear inequality constraints (Veraart et al., 2011) and posed along 60 directions of a densely sampled hemisphere. In particular, the constrained NLS estimator can be written as:

$$\hat{\boldsymbol{\theta}} = \arg\min_{\boldsymbol{\theta}} \varepsilon_{\text{NLS}}(\boldsymbol{\theta}), \tag{11}$$

such that:

$$\boldsymbol{C}\hat{\boldsymbol{\theta}} \leq \boldsymbol{0}, \tag{12}$$

where $\boldsymbol{C}$ is a matrix defining the linear inequality constraints. The initial values for the diffusion and the scaled kurtosis parameters (i.e., $K_{ijkl} = \text{MD}^2 W_{ijkl}$) were set to 0.5 for D_{xx}, D_{yy}, D_{zz}, K_{xxxx}, K_{xxyy}, K_{xxzz}, K_{yyyy}, K_{yyzz}, K_{zzzz} and 0 for D_{xy}, D_{xz}, D_{yz}, K_{xxxy}, K_{xxxz}, K_{xxyz}, K_{xyyy}, K_{xyyz}, K_{xyzz}, K_{xzzz}, K_{yyyz}, K_{yzzz}. If not specified otherwise, the lower and upper bounds on the non-DKI model parameters and the corresponding initialization values were chosen as indicated in Table 1.

In Table 1, $\hat{S}_0$ represents the mean of the non-diffusion-weighted (i.e., $b = 0$) images acquired at the lowest echo time (TE = 67 ms). For the two-compartment models, the fitting procedure was repeated for 4 different initial values of f, namely 0, 0.25, 0.5 and 0.75. The final estimates were selected as the ones that produced the smallest value of the objective function (7). This strategy is motivated by the fact that selecting an initial guess for f far from the underlying ground truth value can cause the fitting algorithm to converge to a local minimum. Thus, with this strategy, we can better avoid local minima and obtain more robust parameter estimates.

In real data experiments, we used one TE = 67 ms repetition and the TE = 120 ms repetition when fitting the models that incorporate a TE dependency (T_2-DKI-FWE and T_2-DKI), whereas we used both the TE = 67 ms repetitions when fitting the DKI-FWE model. In this way, all models could be compared with an equal amount of data points. Model fitting routines have been developed by the authors and the code will be made available in open source.

2.4. Simulating the white matter DW signal

In the simulation experiments, the two-compartment WM model proposed by Fieremans et al. (2011) was used to generate realistic DW-MR signals, originating from a single WM fiber bundle. This model assumes that WM consists of two non-exchanging compartments: the intra- and the extra-axonal space. Both compartments are modeled with a compartment-specific diffusion tensor, $\boldsymbol{D}_a$ and $\boldsymbol{D}_e$ respectively, which are characterized by their eigenvalues λ_a and λ_e and linked through the axonal water fraction f_{aw}. The diffusion-weighted WM signal intensity, S_{wm}, can thus be described as:

$$S_{\text{wm}}(b, \boldsymbol{g}; \boldsymbol{D}_a, \boldsymbol{D}_e, f_{\text{aw}}) = S_0\Big(f_{\text{aw}} \exp\big(-b\boldsymbol{g}^T \boldsymbol{D}_a \boldsymbol{g}\big) + (1 - f_{\text{aw}}) \exp\big(-b\boldsymbol{g}^T \boldsymbol{D}_e \boldsymbol{g}\big)\Big). \tag{13}$$

The ground truth values for λ_a, λ_e and f_{aw} were defined in accordance with the ranges reported in (Fieremans et al., 2011), obtained from in vivo measurements in aligned WM fibers. In (Fieremans et al., 2011), the axons were assumed to have a zero radius, effectively setting the transverse diffusivity in the intra-axonal space to zero. However, in our work, the intra-cellular radial diffusivity was allowed to be larger than zero to include possible larger axons in the human brain (Nilsson et al., 2013). The values used to simulate the WM signal were randomly sampled from uniform distributions defined by the lower and upper bounds indicated in Table 2.

Table 2
Lower bounds (lb) and upper bounds (ub) on the simulated eigenvalues (λ_a and λ_e [μm^2/ms]) and axonal water fraction (f_{aw}) used to generate the WM signal.

	lb	ub
$\lambda_{a,1}$	0.85	1.15
$\lambda_{a,2} = \lambda_{a,3}$	0	0.2
$\lambda_{e,1}$	2	2.5
$\lambda_{e,2} = \lambda_{e,3}$	0.6	1
f_{aw}	0.4	0.6

From the simulated WM signals, corresponding ground truth DKI parameters were obtained by fitting the conventional DKI model (4) to the generated signals using a constrained weighted linear least squares (WLS) approach (Veraart et al., 2011). The DKI parameters were subsequently combined into the T_2-DKI-FWE model, see Eq. (2), with ground truth values for f, T_2^{tissue} and T_2^{fw} to simulate the final, noise-free, DW and TE-dependent signal. Unless noted otherwise, the following values were used as default settings to generate the data: $T_2^{\text{tissue}} = 70$ ms, $T_2^{\text{fw}} = 1573$ ms and variable f to simulate different degrees of PVEs due to free water contamination. Acquisition settings for b, $\boldsymbol{g}$, and TE were chosen in line with the real data acquisition.

2.5. Experiments

2.5.1. T_2^{fw} error propagation study

The goal of this first experiment was to evaluate the potential bias induced in the estimation of the T_2-DKI-FWE model parameters, caused by an erroneous approximation of the T_2^{fw} value. As mentioned in Section 2.3, T_2^{fw} was fixed to a literature value during the actual T_2-DKI-FWE model fit, with the aim of improving the robustness of the parameter estimation problem. However, a poor preliminary assumption on the T_2^{fw} value may bias all other model parameter estimates. For this experiment, 500 DW signals of a WM voxel (with varying ground truth parameter values) were simulated as described in Section 2.4. The acquisition settings were chosen in line with the TE-dependent acquisition protocol presented in Section 2.2. During the simulations, the real T_2^{fw} was varied stepwise from 500 ms to 2100 ms (step size 25 ms) according to the range of values reported in the literature (Piechnik et al., 2009; Qin, 2011). Subsequently, without adding noise, all T_2-DKI-FWE model parameters were estimated assuming $T_2^{\text{fw}} = 1573$ ms. In this experiment, the parameter f was initialized to 0.25 and S_{00} to its true value. The T_2-DKI model, although independent of T_2^{fw} specifically, was also fitted to the data for reference. The experiment was repeated for three different underlying ground truth values of the parameter f, i.e., 0.1, 0.2, and 0.3.

2.5.2. Conditioning of the model fitting problem

One of the main potential improvements of T_2-DKI-FWE over DKI-FWE is the better stability of the model parameter estimation. It is known that the DTI-FWE and DKI-FWE parameter estimation problems are ill-conditioned, thus we propose to remedy this by explicitly modeling the T_2-dependency of the signal. A better conditioning of the inverse estimation problem translates into an improved decoupling of the model parameters. To quantitatively illustrate this, we used the Cramér-Rao lower bound (CRLB), which gives insight on the maximal attainable precision of an unbiased parameter estimator and the correlations between the model parameters (Poot et al., 2010). The CRLB matrix is defined as the inverse of the Fisher information matrix $\boldsymbol{I}(\boldsymbol{\theta})$, which can

be expressed as (van den Bos, 2007):

$$\boldsymbol{I}(\boldsymbol{\theta}) = \mathbb{E}\left\{ \frac{\partial \log p(\boldsymbol{y}|\boldsymbol{\theta})}{\partial \boldsymbol{\theta}} \frac{\partial \log p(\boldsymbol{y}|\boldsymbol{\theta})}{\partial \boldsymbol{\theta}^T} \right\}, \quad (14)$$

where $p(\boldsymbol{y}|\boldsymbol{\theta})$ denotes the conditional distribution of the data $\boldsymbol{y}$ given the parameters $\boldsymbol{\theta}$.

In this experiment, the CRLB matrix was derived assuming Gaussian distributed data for the T_2-DKI, DKI-FWE, and T_2-DKI-FWE models. Additionally, the T_2-DKI-FWE model with simultaneous estimation of $\boldsymbol{\theta}_{T_2-\text{DKI}-\text{FWE}}$ and T_2^{fw} was included in the analysis, and such model will be referred to as T_2-DKI-FWE$_{\text{full}}$. The ground truth diffusion and kurtosis tensors were calculated for a single WM voxel as described in Section 2.4. For generating the single-voxel WM signal, the simulated eigenvalues and the axonal water fraction were: $\lambda_{a,1} = 0.87$ μm^2/ms, $\lambda_{a,2} = \lambda_{a,3} = 0.09$ μm^2/ms, $\lambda_{e,1} = 2.19$ μm^2/ms, $\lambda_{e,2} = \lambda_{e,3} = 0.90$ μm^2/ms and $f_{\text{aw}} = 0.43$. Fitting the DKI model (constrained WLS approach) to the simulated signal resulted in a fractional anisotropy (FA) of 0.60, MD of 0.89 μm^2/ms and mean kurtosis (MK) of 0.91. The other ground truth parameters were fixed to the following values: $S_{00} = 10^3$, $T_2^{\text{tissue}} = 70$ ms, $T_2^{\text{fw}} = 1573$ ms and $f = 0.1$. However, for the computation of the CRLB matrix of the DKI-FWE model, the value of f was converted into the corresponding T_2-weighted, TE-dependent free water fraction using the following relationship (Veraart et al., 2018):

$$f_{\text{DKI}-\text{FWE}} = f^* = \frac{f\exp(-\text{TE}/T_2^{\text{fw}})}{(1-f)\exp(-\text{TE}/T_2^{\text{tissue}}) + f\exp(-\text{TE}/T_2^{\text{fw}})}. \quad (15)$$

Similar to f, the parameter S_{00} was scaled according to the following expression:

$$S_{0,\text{DKI}-\text{FWE}} = S_0^* = S_{00}((1-f)\exp(-\text{TE}/T_2^{\text{tissue}}) + f\exp(-\text{TE}/T_2^{\text{fw}})). \quad (16)$$

The acquisition settings (b, $\boldsymbol{g}$ and TE) were chosen in line with the real data protocol for both the TE-dependent and the TE-independent models. The coefficients of variation and the correlation coefficients can be computed from the CRLB matrix obtained for each model. A more detailed description of how the CRLB matrix, the correlation coefficients, and the coefficients of variation were computed can be found in the Appendix.

2.5.3. Model comparison

In this experiment, the performance of the NLS estimator for different diffusion models was compared on both simulated and real data. Figure 1 schematically illustrates how the single-voxel simulation experiments were designed. For the simulation experiments, a single-voxel signal was generated using the T_2-DKI-FWE model with the same underlying ground truth parameters as presented in Section 2.5.2, with the only difference that multiple ground truth values for the parameter f were considered in the range [0, 0.1, ..., 0.6]. Assuming a Rician data distribution, 10^4 noise realizations were simulated with an SNR = 50, where the SNR is defined as the ratio of the noiseless $b = 0$ signal of a pure tissue voxel ($f = 0$) at TE = 67 ms and the standard deviation of the noise. Note that for our simulation settings, an SNR of 50 at TE = 67 ms corresponds to an SNR of 23.45 at TE = 120 ms. The value of the SNR was chosen to roughly match with the average value of the SNR estimated in white matter voxels of the raw in vivo data analyzed in this paper. The SNR of the tissue compartment is proportional to $(1 - f)$, thus it decreases as f increases, meaning that the data will contain less and less (Fisher) information about the tissue parameters to be estimated. Consequently, the estimation of tissue properties at high f values becomes particularly challenging resulting in ever-decreasing estimation precision, up to the point where reliable estimation is no longer possible. Therefore, we consider $f = 0.6$ a reasonable upper bound for our simulation analysis. Three different models were fitted to both simulated data and real data (after applying all the correction steps discussed in Section 2.2): T_2-DKI, DKI-FWE and T_2-DKI-FWE. Specific metrics that are studied include f (only for the two-compartment models), T_2^{tissue} (only for the TE-dependent models), FA, MD, and MK. The performance of the NLS estimator in simulations was assessed in terms of the accuracy and the precision of the metrics of interest.

3. Results

3.1. T_2^{fw} error propagation study

Figure 2 shows the relative error of the T_2-DKI-FWE tissue parameters (tissue signal fraction, FA, MD, MK, and T_2^{tissue}) as a function of the true underlying T_2^{fw}, caused by an erroneous approximation of T_2^{fw} in the model. The relative error is reported for three different ground truth values chosen for the parameter f ($f_{\text{GT}} = 0.1$, 0.2, and 0.3). During the T_2-DKI-FWE model fit, T_2^{fw} was assumed fixed at 1573 ms, which is indicated with a vertical dashed line in Fig. 2, and the optimization was performed as described in Section 2.3.

In Fig. 2(a), the relative error of the T_2-DKI estimates is compared to that of the T_2-DKI-FWE estimates for FA, MD and MK. When the single-compartment model is fitted to the data, an underestimation of FA can be observed ranging from approximately 31% for $f_{\text{GT}} = 0.1$ to approximately 59% for $f_{\text{GT}} = 0.3$, while MD is severely overestimated, with the relative error ranging from 47% to 128% on average for $f_{\text{GT}} = 0.1$ and $f_{\text{GT}} = 0.3$, respectively. More peculiar is the behavior of MK for which we can point out a shift from an overestimation of approximately 13% when $f_{\text{GT}} = 0.1$ to an underestimation of 16% on average when $f_{\text{GT}} = 0.3$. The comparison between T_2-DKI-FWE and T_2-DKI reveals that when the free water partial volume is not accounted for, the bias induced in the estimates of the tissue diffusion metrics is substantially larger compared to the bias caused by inserting a (biased) approximation of T_2^{fw} in the T_2-DKI-FWE model. Figure 2(b) provides a close-up of Fig. 2(a) with a focus on the T_2-DKI-FWE tissue parameters only: the results show a relatively small percent error for most model metrics when $f_{\text{GT}} = 0.1$, even when the true T_2^{fw} is significantly smaller than the model assumption. The largest effect occurs for MK, with an overestimation of approximately 7% in the case of a true $T_2^{\text{fw}} = 500$ ms. On the other hand, the relative error due to an erroneous approximation of T_2^{fw} increases as f_{GT} increases, leading to an overestimation greater than 15% for MK and MD, an overestimation of approximately 9% for the tissue signal fraction $(1 - f)$ and an FA underestimation of approximately 13% in the case of a true $T_2^{\text{fw}} = 500$ ms and $f_{\text{GT}} = 0.3$.

3.2. Conditioning of the model fitting problem

In Fig. 3, the absolute coefficients of variation and the absolute correlation coefficients derived from the CRLB matrix are shown for the four models of interest: T_2-DKI, DKI-FWE, T_2-DKI-FWE and T_2-DKI-FWE$_{\text{full}}$. The CRLB matrix was obtained by inverting the Fisher information matrix and assuming Gaussian distributed data with an SNR of 50. By fixing the SNR, the corresponding noise level σ was computed as $\sigma = S_{00}\exp(-\text{TE}/T_2^{\text{tissue}})/\text{SNR}$ and resulted in a value of 7.68 given $S_{00} = 10^3$, $T_2^{\text{tissue}} = 70$ ms and TE = 67 ms.

Although the T_2-DKI model leads to lower absolute correlation coefficients (off-diagonal elements in Fig. 3) between the different parameters compared to the bi-compartment models, the single-compartment model does not allow us to account and thus to correct for PVEs. The highest correlation coefficients are instead obtained for the T_2-DKI-FWE$_{\text{full}}$ model which implies T_2^{fw} as an additional parameter to be estimated. The comparison between DKI-FWE and T_2-DKI-FWE in terms of correlation coefficients highlights that the incorporation of the compartment-specific T_2 relaxation terms with T_2^{fw} assumed known a priori is beneficial for the identifiability (lower correlations) of the different parameters. The CRLB analysis of both T_2-DKI-FWE and DKI-FWE shows high correlations between f (or f^*) and D_{xx} and D_{yy}. More specifically, when the DKI-FWE model is considered, the absolute correlation coefficient $|r_{f^*,D_{yy}}|$ is found to be as high as 0.96, while for the T_2-DKI-FWE model $|r_{f,D_{yy}}|$ decreases to 0.84. Correlated estimates of f and D_{xx} and D_{yy}

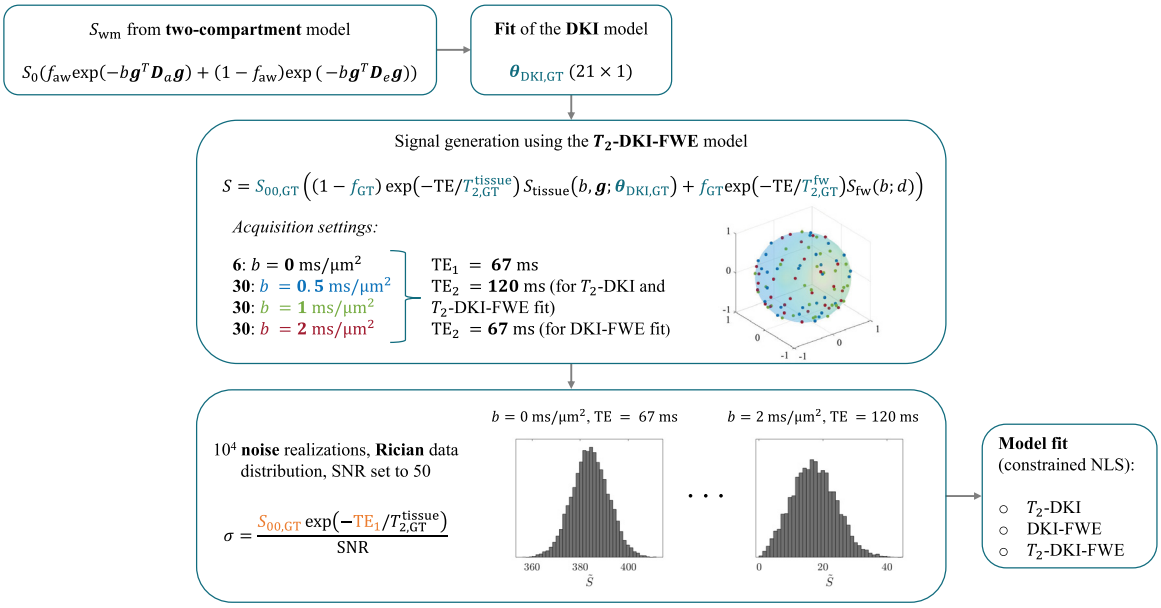

Fig. 1. Flowchart of the single-voxel simulation experiments. First, ground truth DKI parameters are obtained by fitting the DKI model to the signal S_{wm}, representative of a single WM voxel. Subsequently, the T_2-DKI-FWE model is used to generate diffusion-weighted signals with variable or single TE and the following ground truth values: $S_{00,GT} = 10^3$, $T^{tissue}_{2,GT} = 70$ ms, $T^{fw}_{2,GT} = 1573$ ms and f_{GT} in the range from 0 to 0.6 (0.1 step size). Next, the generated data are corrupted with noise according to a Rician data distribution and an SNR of 50 defined on the non-diffusion-weighted signal of a pure tissue voxel at the lowest TE, i.e., 67 ms. Finally, the T_2-DKI and the T_2-DKI-FWE models are fitted to the data generated with variable TE ($TE_1 = 67$ ms and $TE_2 = 120$ ms), while the DKI-FWE model is fitted to the single-TE data ($TE_1 = TE_2 = 67$ ms). The diffusion weighting directions are displayed on the unit sphere as colored dots, where the different colors reflect the corresponding b-values. $\tilde{S}$ denotes the noisy signal.

will result in correlated estimates of f and MD. However, our CRLB results predict a less strong correlation between f and MD for T_2-DKI-FWE than for DKI-FWE. The better decoupling of the free water fraction from the other model parameters is also confirmed by the mean absolute correlation coefficient between f (or f^*) and the other parameters: 0.38 for DKI-FWE and 0.29 for T_2-DKI-FWE. From Fig. 3, it is clear that high correlations also exist between some diffusion and kurtosis tensor elements, e.g., between K_{yyyy} and D_{yy} and between K_{xxxx} and D_{xx}. Yet, in both cases, T_2-DKI-FWE produces lower correlations compared to DKI-FWE (0.90 vs 0.96 for K_{yyyy} and D_{yy} and 0.88 vs 0.95 for K_{xxxx} and D_{xx}, respectively).

To quantitatively summarize the differences between the models, we propose a scalar measure that quantifies the correlation between the elements of a subset of parameters. It is calculated as the mean of their mutual correlation coefficients that were derived from the CRLB matrix, i.e., the mean of the corresponding off-diagonal elements of the matrix shown in Fig. 3. The models T_2-DKI-FWE$_{full}$ and T_2-DKI are not included in this quantitative analysis since the first one is severely ill-conditioned and the latter one can be seen as a particular case of the T_2-DKI-FWE model when $f = 0$. Two subsets of parameters are considered of particular interest for our analysis:

1. $\boldsymbol{\theta}_{S1} = [\boldsymbol{\theta}_D, \boldsymbol{\theta}_K, f]$ for T_2-DKI-FWE and $\boldsymbol{\theta}_{S1} = [\boldsymbol{\theta}_D, \boldsymbol{\theta}_K, f^*]$ for DKI-FWE;
2. $\boldsymbol{\theta}_{S2} = [\boldsymbol{\theta}_D, \boldsymbol{\theta}_K]$.

The values of the scalar measure for the models of interest are reported in Table 3.

The results in Table 3 confirm that, on average, the T_2-DKI-FWE parameters of interest are less correlated compared to the DKI-FWE parameters. As a further validation, we repeated our CRLB analysis on two additional parameter sets, the results of which are included in Section A of the supplementary material. More specifically, the matrices of the correlation coefficients and coefficients of variation are shown for:

Table 3
Mean of the absolute mutual correlation coefficients derived from the DKI-FWE and T_2-DKI-FWE CRLB matrices for the parameter sets $\boldsymbol{\theta}_{S1}$ and $\boldsymbol{\theta}_{S2}$.

Metric	Parameter set	DKI-FWE	T_2-DKI-FWE
Mean of off-diagonal elements	$\boldsymbol{\theta}_{S1}$	**0.2002**	**0.1385**
	$\boldsymbol{\theta}_{S2}$	0.1818	**0.1258**

1. a voxel with the same diffusion and relaxation properties as the ones discussed in Section 2.5.2 but with a higher underlying free water signal fraction, i.e., $f = 0.5$ (Fig. S1);
2. a voxel with the same free water fraction as the one originally selected ($f = 0.1$) but with different diffusion properties to cover a wider range of realistic diffusional kurtosis estimates (Lätt et al., 2013): FA = 0.70, MD = 0.75 μm²/ms and MK = 1.12 (Fig. S2).

Given the severe ill-conditionedness of T_2-DKI-FWE$_{full}$, this model was not included in the simulation and real data experiments carried out to evaluate the performance of the NLS estimator (Section 3.3).

3.3. Model comparison

3.3.1. Simulation experiments

In this set of experiments, the following diffusion models are compared in a Monte Carlo simulation framework: T_2-DKI, DKI-FWE and T_2-DKI-FWE. The results obtained from the single-voxel simulation experiments for $f_{GT} = 0.1$, 0.2 and 0.3 are shown in Figs. 4 and 5, where the error distributions of the metrics of interest are given for each model. The error terms were computed as $\hat{p}_i - p_{GT}$ where $\hat{p}_i$ is the parameter estimate associated with the i^{th} repetition of the experiment and p_{GT} is the ground truth value of the same parameter.

It is clear from Fig. 4 that the T_2-DKI model is biased and overestimates MD while underestimating FA. It is also noticeable that the effect of partial volumes tends to translate into an overestimated MK for lower f values (0.1) and an underestimated MK for higher f values (0.2

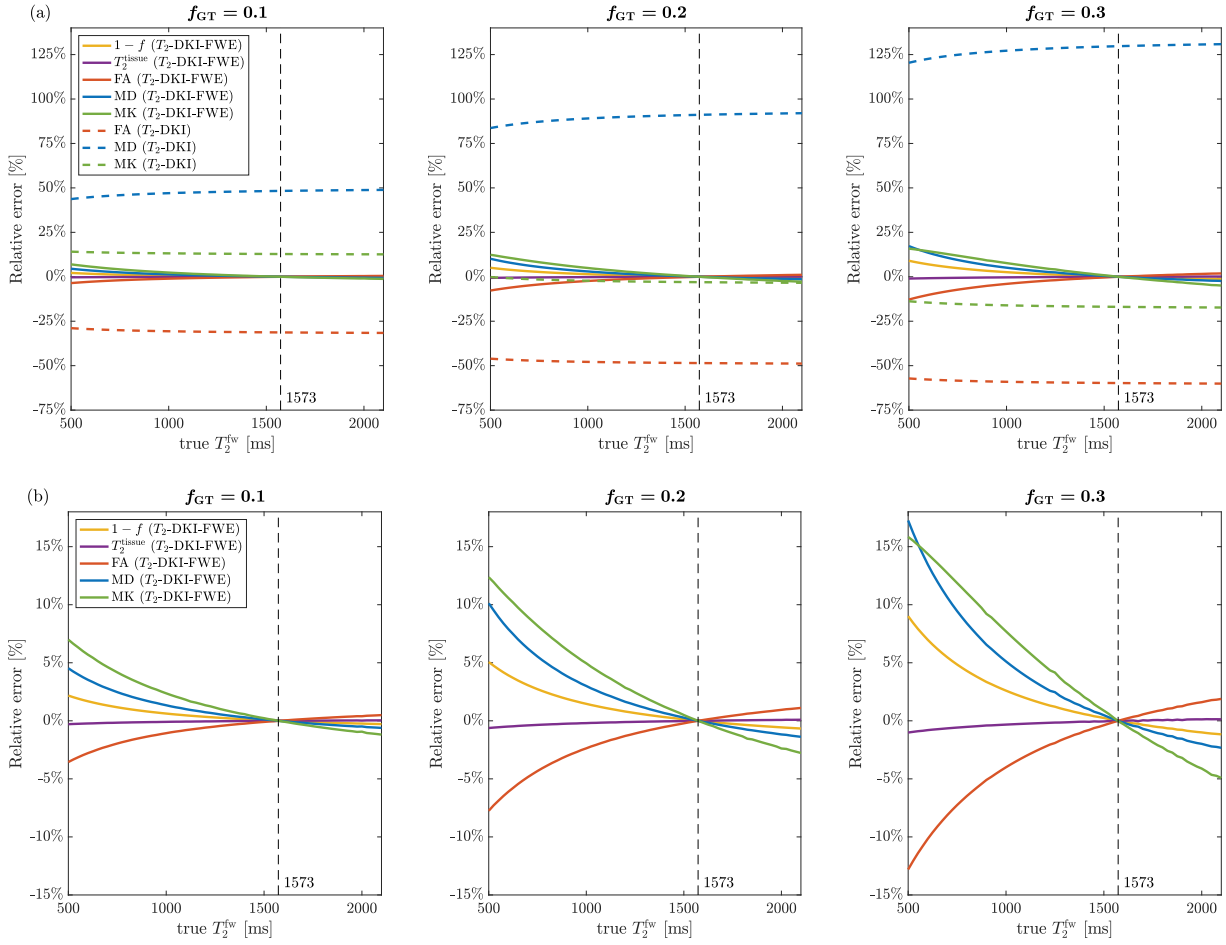

Fig. 2. Propagation of the relative error of the analyzed model metrics: the tissue signal fraction $(1 - f)$, FA, MD, MK, and T_2^{tissue} as a function of the true T_2^{fw} and for three different ground truth values of the free water fraction f_{GT} (0.1 left, 0.2 center and 0.3 right). Full lines denote the errors on the T_2-DKI-FWE parameter estimates assuming $T_2^{fw} = 1573$ ms, while the dashed lines denote the errors on the T_2-DKI estimates. Figure (b) shows a close-up of figure (a) with a focus on the T_2-DKI-FWE parameter estimates.

and 0.3). This is confirmed by the mean value of the MK error distributions obtained for the T_2-DKI model: 0.0328 for $f_{GT} = 0.1$, −0.0920 for $f_{GT} = 0.2$ and −0.2033 for $f_{GT} = 0.3$. The f value for which the MK underestimation effect becomes noticeable depends on the underlying ground truth value of the metric as pointed out in noise-free simulations discussed in Section B of the supplementary material.

Although biased, the single-compartment T_2-DKI model achieves the highest precision. Given the higher precision and the relatively small bias of the MK estimates, T_2-DKI outperforms T_2-DKI-FWE in terms of the mean squared error (MSE) of MK when f_{GT} is 0.1 (0.0013 vs 0.0055, respectively). In contrast, starting from $f_{GT} = 0.2$, the T_2-DKI-FWE model results in a lower MSE of MK compared to T_2-DKI due to the more significant negative bias in the T_2-DKI MK estimates. Fig. 5 shows the error distributions for f and T_2^{tissue}, where the DKI-FWE f estimates are corrected for the T_2 bias using the relationship presented in Eq. (15). The ground truth T_2 values of tissue and free water were used to make the correction. The parameter f is estimated with a lower precision when using the DKI-FWE model compared to T_2-DKI-FWE (Fig. 5(a)) and T_2^{tissue} is significantly overestimated by T_2-DKI (Fig. 5(b)). While Figs. 4 and 5 show results for f values up to and including 0.3, larger values of f can also be observed in in vivo data, especially in voxels located at the border of the lateral ventricles. Therefore, Fig. 6 shows the performance of T_2-DKI-FWE and DKI-FWE in terms of bias, variance and MSE of the diffusion-related metrics for f values up to and including 0.6. The T_2-DKI model has not been included in this comparative plot since its performance was found to be inferior. This is because it produces parameter estimates that suffer from a severe bias (cf. Fig. 4), which becomes larger with an increasing value of f.

Our results suggest that the bias of FA, MD, and MK is relatively low in the analyzed range of f values and thus, the precision of the parameter estimates becomes the dominant factor when assessing the performance of the models in terms of the MSE. In the whole f range (from 0 to 0.6) and for all three metrics, the T_2-DKI-FWE model fits resulted in lower MSE values compared to the DKI-FWE model. We also observed that the DKI-FWE model fitting produced different results at $f = 0.6$ when using different initial guesses in the optimization routine, which suggests an increased risk that the global optimum is not found. The MSE of FA, MD, and MK for all three models in the analyzed range of f values can be found in Table S2 (Section C of the supplementary material).

To conclude our simulation analysis, Figs. 7(a) and (b) provide a scatter plot of the DKI-FWE and T_2-DKI-FWE estimates of f versus MD and of MD versus MK for $f_{GT} = 0.1$, respectively. As previously described, the DKI-FWE f estimates were corrected for the T_2 bias. From Fig. 7(a), it is clear that the scatter plot for the T_2-DKI-FWE model is less elongated compared to that of the DKI-FWE model, indicating a smaller correlation between f and MD. This is confirmed by the Pearson correlation coefficients, which are: $R = -0.91$ for the T_2-DKI-FWE model and $R = -0.98$ for DKI-FWE. Note that there still exists a strong correlation between f and MD when using the T_2-DKI-FWE model, however, the two parameters are better decoupled and more precisely estimated compared to DKI-FWE. Similarly, Fig. 7(b) high-

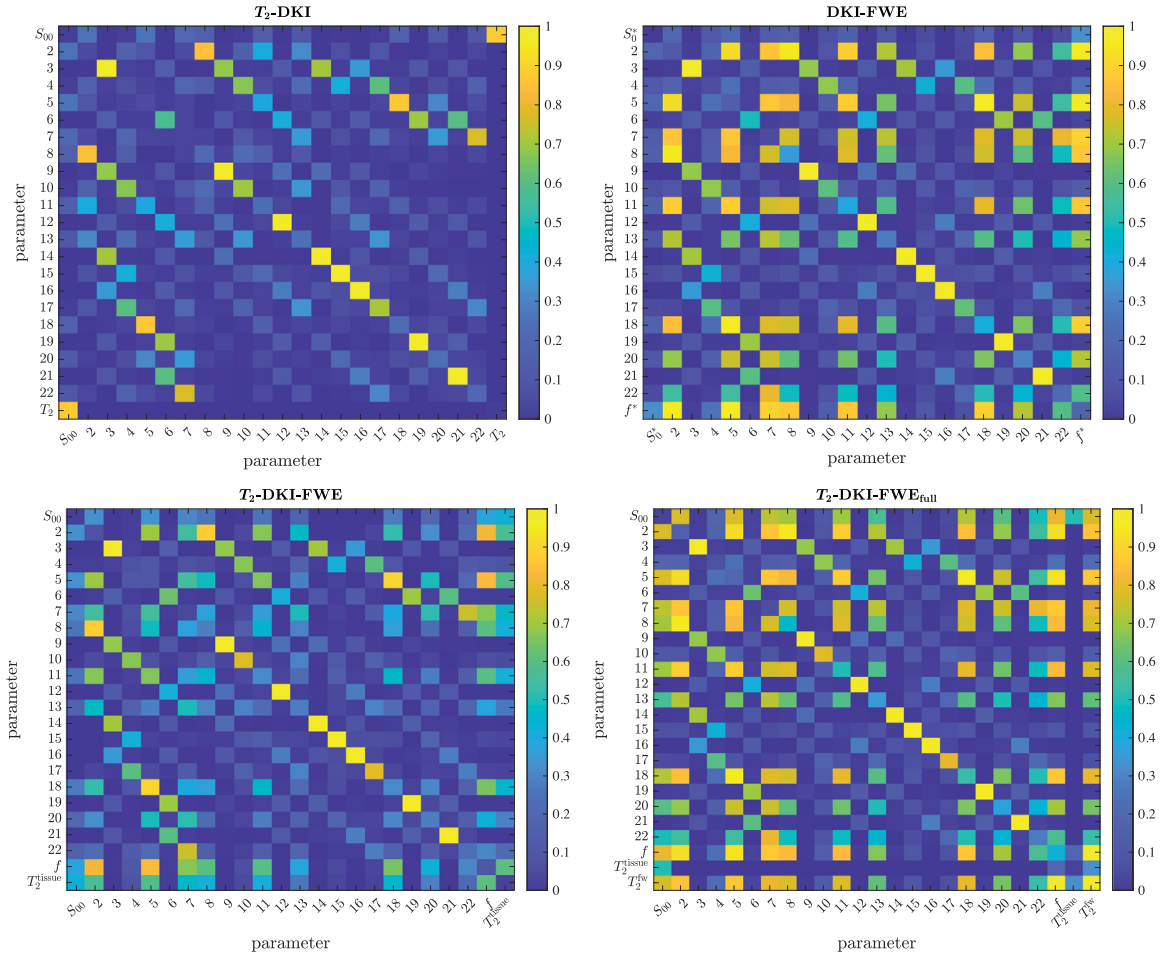

Fig. 3. Absolute values of the correlation coefficients (off-diagonal elements) and coefficients of variation (main diagonal elements), derived from the CRLB matrix, for the T_2-DKI, DKI-FWE, T_2-DKI-FWE and T_2-DKI-FWE$_{full}$ models. Parameters from 2 to 22 are the same for all models: D_{xx} (2), D_{xy} (3), D_{xz} (4), D_{yy} (5), D_{yz} (6), D_{zz} (7), K_{xxxx} (8), K_{xxxy} (9), K_{xxxz} (10), K_{xxyy} (11), K_{xxyz} (12), K_{xxzz} (13), K_{xyyy} (14), K_{xyyz} (15), K_{xyzz} (16), K_{xzzz} (17), K_{yyyy} (18), K_{yyyz} (19), K_{yyzz} (20), K_{yzzz} (21), K_{zzzz} (22). The free water fraction was 0.1 for the models incorporating T_2 relaxation (namely T_2-DKI-FWE and T_2-DKI-FWE$_{full}$) and converted to its TE-dependent version for the DKI-FWE model ($f^* = 0.22$). For the models with explicit T_2 dependency, S_{00} was set to 10^3, while for DKI-FWE, S_0^* resulted in a value of 441.42. $T_2^{tissue} = 70$ ms and $T_2^{fw} = 1573$ ms were assumed. The highest coefficients of variation were clipped to 1 for the sake of visualization.

lights that MD and MK are less correlated and can be estimated with higher precision by T_2-DKI-FWE. These results are in line with the findings of the CRLB analysis (Section 3.2). The Pearson correlation coefficients between f and MD and between MD and MK for the analyzed range of f values are presented in section C of the supplementary file (Table S3).

3.3.2. Real data experiments

The real data analysis was performed in WM voxels of a region of interest (ROI) made up of 8 axial slices where PVEs are likely to be observed. The WM mask was extracted using a thresholding approach after applying multi-shell multi-tissue (MSMT) constrained spherical deconvolution (CSD) (Jeurissen et al., 2014) to the diffusion-weighted images acquired at the lowest TE, i.e., 67 ms. We assessed the tissue-related model metrics in voxels for which the free water signal fraction f estimated by T_2-DKI-FWE was lower than 0.6. For higher f values, the tissue-specific metrics start to become meaningless due to the insufficient tissue signal contribution. Additionally, the MK estimates in voxels corresponding to such high f estimates often resulted in outlier values (either extremely low or extremely large). Thus, the exclusion of the voxels for which $f > 0.6$ (0.39% of the total number of voxels included in the fitting) was beneficial in terms of visualization. The real data maps are shown in Fig. 8 for one slice of the selected ROI. A visual indication of the spatial location where the estimated parameters were close to the posed constraints can be found in the supplementary material (section D, Fig. S5). When comparing T_2-DKI-FWE and DKI-FWE, in Figs. 8(c) and (b), we notice that DKI-FWE produces larger f values, which is in line with the simulation results. Furthermore, relevant differences are captured by the diffusion-related parameter maps (FA, MD, and MK). Compared to T_2-DKI, in the genu of the corpus callosum we observe a reduced effect of free water partial volumes on the metrics of interest when T_2-DKI-FWE or DKI-FWE are used: in this area we can in fact highlight more plausible higher FA and MK values while lower MD and T_2^{tissue} values.

The comparison between T_2-DKI and T_2-DKI-FWE is also illustrated in the histograms in Fig. 9 where we report the distributions of the metrics of interest for the same slice as the one shown in Fig. 8 and for voxels affected by a certain degree of free water contamination ($0.05 \leq f \leq 0.6$). The results in Fig. 9 confirm the trends observed in our simulation analysis: when using the single-compartment T_2-DKI model, FA results in lower values compared to the T_2-DKI-FWE estimates while MD and T_2^{tissue} are significantly higher, often resulting in implausibly large values (greater than 3 μm^2/ms for MD and greater than 200 ms for T_2^{tissue}). Finally, no clear shift of the distribution of the T_2-DKI MK estimates can be highlighted suggesting, in agreement with simulations, that the effect of partial volumes on MK depends on both the level of

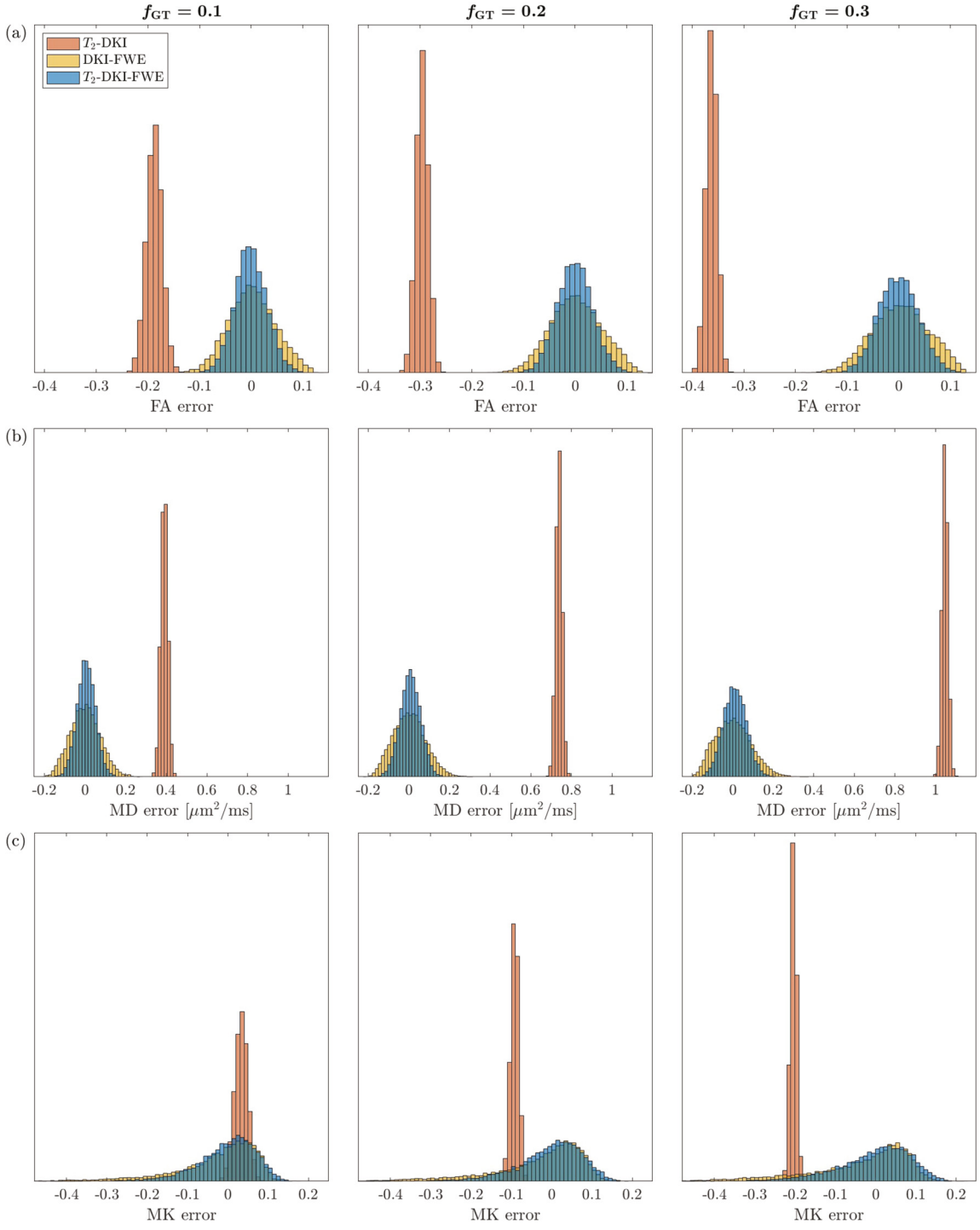

Fig. 4. Error distributions of the diffusion-related metrics of interest for three different ground truth values of the free water fraction f_{GT} (0.1 left, 0.2 center and 0.3 right): (a) fractional anisotropy (FA), (b) mean diffusivity (MD) and (c) mean kurtosis (MK). The error distributions are compared for the three models discussed in this work: T_2-DKI (orange bins), DKI-FWE (yellow bins), and T_2-DKI-FWE (blue bins).

free water contamination and on the actual underlying value (unknown for real data). The distributions of the metrics of interest for all three models are shown in Section D of the supplementary material for both voxels not affected by PVEs (Fig. S6) and contaminated voxels (Fig. S7). Interestingly, Fig. 9 shows that MK and FA are more widely distributed for the T_2-DKI-FWE model compared to T_2-DKI and we hypothesize that when the model fit is performed using the bi-compartment model, the observed distributions are more likely to capture the actual variability of FA and MK observed in the tissue while the T_2-DKI parameter estimates are confounded by PVEs. Our ROI was intentionally selected to include in the analysis voxels for which free water contamination is likely to be observed. Consequently, the analyzed ROI contains a variety of voxels with different diffusion profiles: highly coherent white matter structures as well as voxels for which the underlying diffusion properties are more similar to gray matter structures. While MD shows a lower variability across adult brain tissue (Beaulieu, 2014), the different degree of anisotropy is expected to result in wider FA and MK distributions that reflect the heterogeneous diffusion characteristics of the analyzed

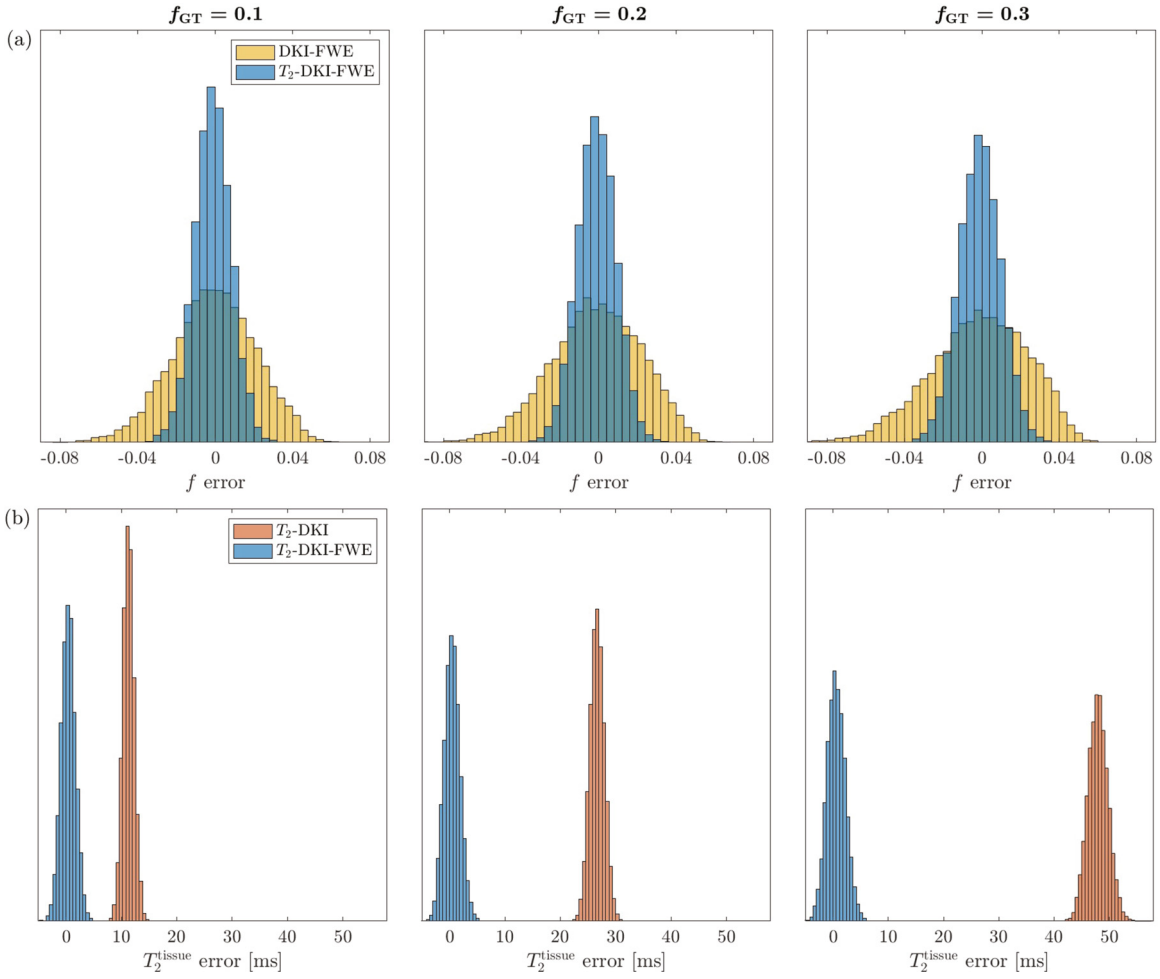

Fig. 5. Error distributions of f (a) and T_2^{tissue} (b) for three different ground truth values of the free water fraction f_{GT} (0.1 left, 0.2 center and 0.3 right). In (a) the DKI-FWE estimates of f are corrected for the T_2 bias using the true T_2^{tissue} and T_2^{fw} values. When looking at f, the error distributions are compared for DKI-FWE (yellow bins) and T_2-DKI-FWE (blue bins), whereas for T_2^{tissue} the error terms from T_2-DKI (orange bins) and T_2-DKI-FWE (blue bins) are assessed.

voxels. As an additional validation, we show that the distributions of FA and MK observed in real data can be reproduced to a good extent when fitting the T_2-DKI-FWE and the T_2-DKI models to synthetic data, retrospectively generated from the T_2-DKI-FWE parameter estimates (cf. Fig. S8, Section D of the supplementary material).

4. Discussion

4.1. Motivation

The beneficial effects of accounting for PVEs in dMRI data through a bi-compartment model have already been extensively described in the literature, including applications on schizophrenia (Pasternak et al., 2012), aging (Metzler-Baddeley et al., 2011; Sasson et al., 2013) and Alzheimer's disease (Bergamino et al., 2021; Hoy et al., 2017). Because it is known that DKI provides a better description of the diffusion process in brain tissue compared to DTI, we use the DKI model to represent the tissue compartment. However, the combination of the bi-exponential FWE model with DKI leads to a severely ill-conditioned parameter estimation problem (Collier et al., 2018). Such ill-conditionedness may be mitigated through advanced parameter estimation techniques and the use of statistical priors (Collier et al., 2018), having as a drawback that these types of prior information can potentially bias the parameter estimates.

As a solution to this drawback, we introduce the bi-exponential T_2-DKI-FWE diffusion model which eliminates free water PVEs by separating the signal contributions of the tissue and free water compartments, while explicitly accounting for the different compartmental T_2. In simulation experiments, we show how not accounting for this free water partial volume effect can severely bias tissue-related diffusion and relaxometry metrics, leading to an underestimation of FA, and an overestimation of MD and T_2^{tissue} (Figs. 4 and 5). When estimating MK in WM voxels without correcting for free water partial volumes, our findings reveal an interesting behavior consisting of a shift from over- to underestimation of the actual underlying MK. The comparison between the MK estimates obtained from T_2-DKI and the ones extracted by T_2-DKI-FWE shows that the metric starts to be underestimated from free water fraction values close to 0.2, although this value depends on the actual underlying θ_{DKI} (cf. Table S1 and Fig. S3 of the supplementary file). We can thus refer to overestimation as the effect of partial volumes on MK at a low f regime and to underestimation as the effect at a high f regime. In previous work (Collier et al., 2018), however, only an overestimation of MK has been reported to be the consequence of not accounting for PVEs, and therefore it is important to highlight the main differences between our work and (Collier et al., 2018). In the current study, we explicitly model the T_2 relaxation terms of both compartments of interest, whereas in (Collier et al., 2018) the conventional DKI model is compared to DKI-FWE and, in simulations, a distribution of free water

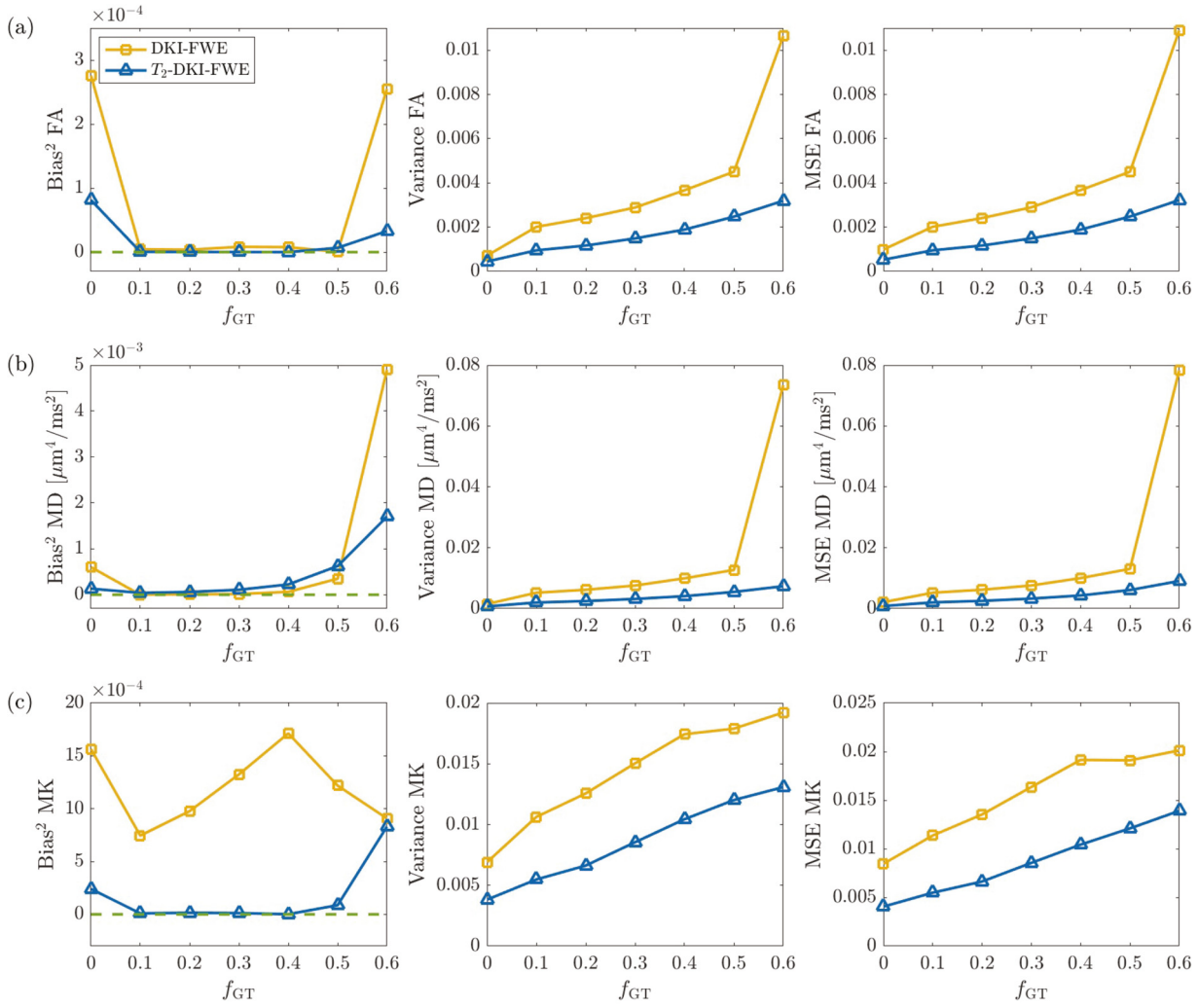

Fig. 6. Squared bias, variance and mean squared error (MSE) of the diffusion-related parameters as a function of the underlying ground truth free water signal fraction f_{GT}: (a) fractional anisotropy (FA), (b) mean diffusivity (MD) and (c) mean kurtosis (MK). The DKI-FWE (yellow curves) and the T_2-DKI-FWE (blue curves) models are compared. In the left column, displaying the squared bias of the metrics of interest, a green dashed line is shown as reference (unbiased).

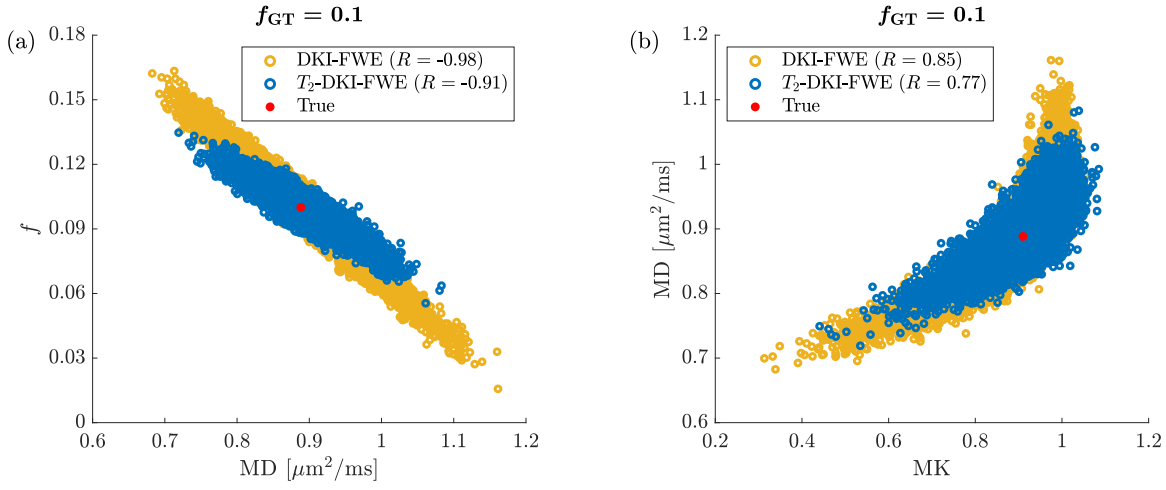

Fig. 7. (a) Scatter plot of the DKI-FWE (yellow) and T_2-DKI-FWE (blue) estimates of f versus MD. The DKI-FWE estimates of f are corrected for the T_2 bias using the true T_2^{tissue} and T_2^{fw} values. (b) Scatter plot of the DKI-FWE (yellow) and T_2-DKI-FWE (blue) estimates of MD versus MK. Ground truth values are indicated by a red dot. The results are given for an underlying free water fraction (f_{GT}) of 0.1 and the corresponding Pearson correlation coefficients are shown in the legend.

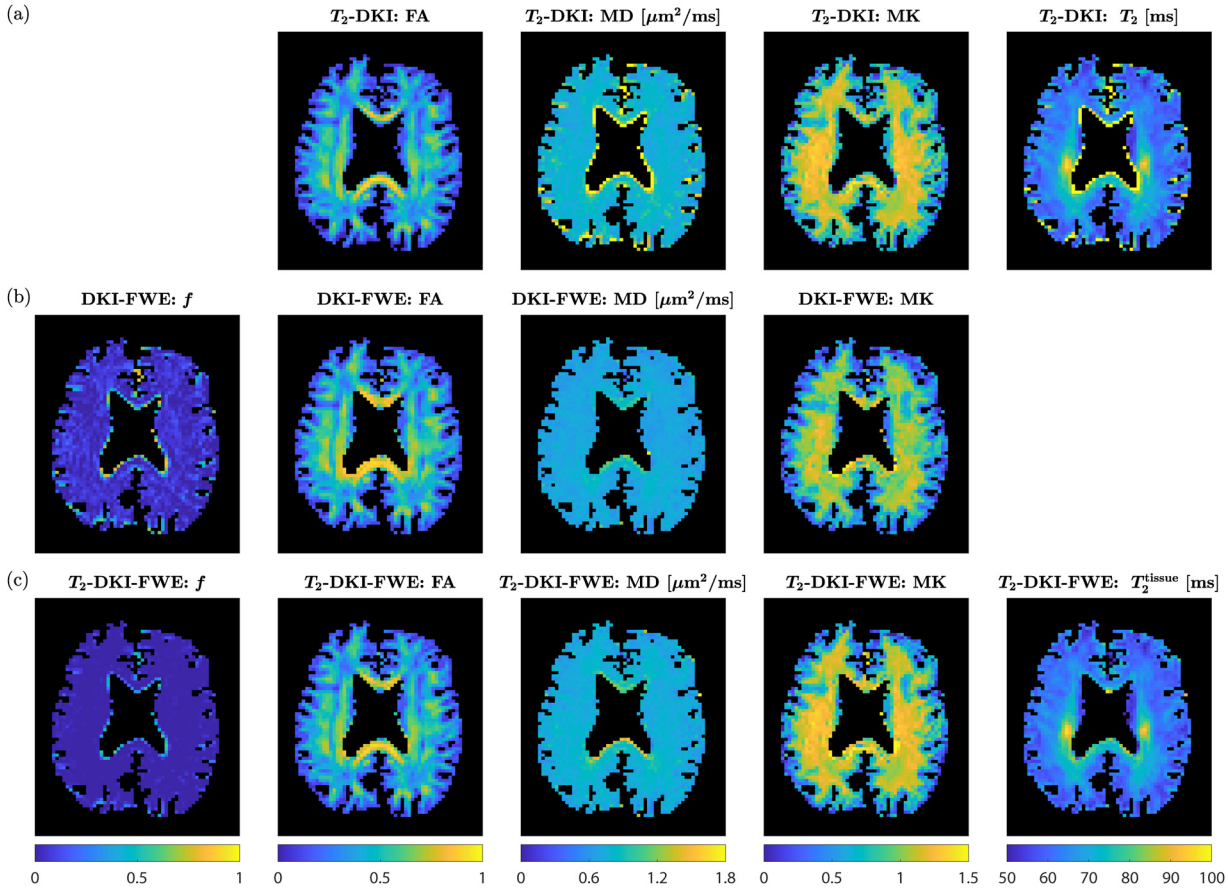

Fig. 8. Real data maps of the metrics of interest (f, FA, MD, MK and T_2^{tissue}) for one slice of the analyzed in vivo data and the three models discussed in this work: (a) T_2-DKI, (b) DKI-FWE and (c) T_2-DKI-FWE.

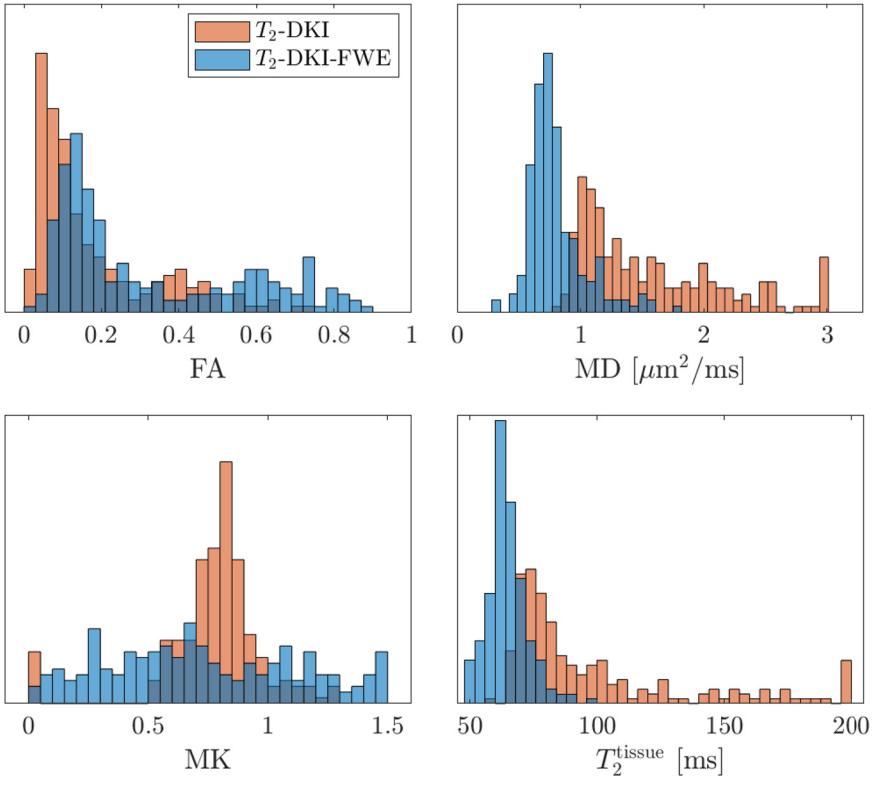

Fig. 9. Distributions of the metrics of interest (FA, MD, MK, and T_2^{tissue}) for one slice of the analyzed in vivo data and for voxels affected by free water contamination ($0.05 \leq f \leq 0.6$). The estimates obtained from the T_2-DKI (orange bins) and the T_2-DKI-FWE (blue bins) model fitting are compared. Outlier values have been clipped for the sake of visualization.

fractions with mean 0.26 and standard deviation 0.24 was chosen. Given that f in the DKI-FWE model represents a T_2-weighted signal fraction, the transition between the low regime effect and the high regime effect occurs at higher f values (cf. Table S1 and Fig. S4 of the supplementary file) making overestimation the most pronounced tendency for the considered f distribution. Furthermore, the different estimation technique might also play a role: in this work we use a constrained NLS approach as opposed to (Collier et al., 2018) where a Bayesian estimation framework is proposed.

4.2. Incorporating T_2 relaxation properties

To stabilize the ill-conditioned DKI-FWE parameter estimation problem, we include compartment-specific T_2 relaxation properties. Our CRLB analysis shows in fact how the absolute correlation coefficients between the different model parameters become lower when the T_2-DKI-FWE model is used compared to DKI-FWE (Fig. 3 and Table 3), thus indicating a better decoupling of the different parameters and hence an improved conditioning of the model fitting problem. These findings are confirmed by our Monte Carlo simulation experiments, where we observed that the introduction of the T_2 relaxation terms into the DKI-FWE model yields less correlated and more precise parameter estimates (Figs. 6 and 7).

An important consequence of including the compartment-specific T_2 relaxation properties consists in the fact that now, the parameter f will no longer incorporate the T_2-weighting term (Farrher et al., 2020; Jerome et al., 2016; Veraart et al., 2018), as opposed to the f extracted from DKI-FWE (see Eq. (15)). Even though T_2-DKI-FWE accounts for the different T_2 relaxations of tissue and free water, the parameter f still needs to be regarded as a signal fraction, and not as a volume fraction, because the different proton densities and T_1 properties of the two compartments are not explicitly modeled. Finally, the T_2-DKI-FWE model also provides the tissue-specific T_2^{tissue} parameter, thereby yielding an additional potential biomarker.

4.3. Model assumptions, limitations and future perspectives

We showed that explicitly estimating T_2^{fw} as an additional parameter negatively impacts the conditioning of the model fitting (see Fig. 3 T_2-DKI-FWE$_{\text{full}}$). Therefore, during the T_2-DKI-FWE model fit, T_2^{fw} is not estimated together with the other model parameters but fixed to its literature value of 1573 ms (Qin, 2011). Alternatively, T_2^{fw} could be estimated before the fitting procedure, however, this would require the acquisition of multiple extra $b = 0$ images with a very wide range of TEs to precisely capture the long T_2 of the free water compartment. For these reasons, a fixed T_2^{fw} value is used to avoid the parameter estimation problem becoming even more ill-conditioned compared to the DKI-FWE model (Collier et al., 2017). As a downside, making an erroneous choice for T_2^{fw} will bias the other parameter estimates (see Fig. 2). This bias increases as the free water fraction f increases and is larger for MK and MD. Fortunately, considering an over- or underestimation of our fixed T_2^{fw} by 500 ms and f_{GT} variable from 0.1 to 0.3, the error introduced in the tissue-related metrics stays between −4% and +7.7%, with the lower and upper bounds obtained for FA and MK respectively when $T_2^{\text{fw}} = 1000$ ms and $f_{\text{GT}} = 0.3$. Despite the introduced error, keeping T_2^{fw} fixed to a reference value seems the most reasonable choice to prevent the model degeneracy that estimating it as an additional parameter would imply.

Another implicit model assumption is that T_1 is the same for both compartments, which is not the case as typical T_1 values reported in the literature at 3 T vary from 728 to 1735 ms for WM and from 3817 to 6837 ms for CSF (Bojorquez et al., 2017). Incorporating and subsequently estimating T_1 properties into the model would result in a more extensive acquisition protocol, as multiple repetition times would then be required. Moreover, depending on which T_1 we would try to estimate, the conditioning of the parameter estimation problem might be negatively affected, thus losing the benefits given by the incorporation of the T_2 relaxation terms. When using T_1 values reported in the literature instead of estimating them, the multi-TR acquisition protocol would no longer be necessary, however, we would run the risk of introducing an additional source of bias when T_1 values are not chosen correctly. Further research on the impact of incorporating T_1 properties is thus required, before including the longitudinal relaxation term in the model.

Furthermore, it should be reported that when fitting the discussed models to real datasets, we observed a few implausible outliers in the MK estimates (all models) and MD estimates (mainly T_2-DKI). This may be the result of a combination of factors including model complexity, noise sensitivity, and imaging artifacts, but further investigation is needed to identify the exact cause.

Finally, we would like to point out that nowadays multi-TE diffusion datasets are rarely acquired in clinical practice, implying that *ad hoc* acquisitions would be needed to benefit from the approach presented in this work. Even when diffusion data acquired with multiple TEs are available, it is important to keep in mind that most clinical scanners offer no control over the DW gradient amplitude, and consequently over the diffusion time Δ which is typically around 30 to 60 ms. When acquiring multiple TEs, it is likely that Δ changes between TEs, thus impacting the diffusion parameters. Based on the work of (Fieremans et al., 2016), the axial and radial diffusivities in human white matter show a pronounced and weaker diffusion time dependency, respectively. In other studies, the effect of the diffusion time, in the range of 30–60 ms, on diffusion tensor-derived metrics is considered negligible (Clark et al., 2001; Le Bihan et al., 1993). In future work, the diffusion time dependency of the T_2-DKI-FWE model should be thoroughly explored. Therefore, if available, acquisition protocols that allow for constant Δ with varying TEs are advised to avoid a potential source of bias. While ensuring a constant Δ could be beneficial in terms of bias reduction, using optimal b-values and TEs may maximize the precision of the diffusion parameter estimates. Therefore, in future work, we aim to optimize the data acquisition in terms of the precision with which the parameters of interest can be estimated by using CRLB-based optimality criteria.

5. Conclusions

In conclusion, incorporating T_2 relaxation properties in the ill-conditioned DKI-FWE model ensures a better conditioning of the parameter estimation problem, while only requiring the use of at least two different TEs in the acquisition phase. We show that by doing so, precise and accurate parameter estimates relating to the diffusion properties of the tissue can be obtained using standard estimation techniques like a constrained NLS estimator without regularization. In addition to partial volume corrected diffusion metrics, a further benefit of the presented approach includes the modeling of an additional clinically relevant tissue-related parameter, T_2^{tissue}.

Data and code availability statement

In vivo data used in this work will be available via a formal request to the corresponding author and a data sharing agreement should be signed by both parties. Real data pre-processing was performed using the MRtrix3 software framework (Tournier et al., 2019). Model fitting routines have been developed by the authors and the code will be made available in open source.

Declaration of Competing Interest

VA has a collaboration agreement with ico**metrix**. JV is co-inventor of a patent on the denoising methodology that was used in this study (US10698065B2). TB is employee of ico**metrix**. The remaining authors declare that the research was conducted in the absence of any com-

mercial or financial relationships that could be construed as a potential conflict of interest.

Credit authorship contribution statement

Vincenzo Anania: Methodology, Data curation, Formal analysis, Investigation, Software, Writing – original draft, Writing – review & editing. **Quinten Collier:** Methodology, Formal analysis, Investigation, Software, Writing – original draft. **Jelle Veraart:** Methodology, Formal analysis, Software, Writing – review & editing, Supervision. **Annemieke E. Buikema:** Formal analysis, Methodology, Writing – review & editing. **Floris Vanhevel:** Investigation, Data curation. **Thibo Billiet:** Formal analysis, Methodology, Writing – review & editing. **Ben Jeurissen:** Conceptualization, Methodology, Formal analysis, Software, Writing – review & editing, Supervision. **Arnold J. den Dekker:** Conceptualization, Methodology, Formal analysis, Writing – review & editing, Supervision. **Jan Sijbers:** Conceptualization, Methodology, Formal analysis, Writing – review & editing, Supervision.

Acknowledgment

This project has received funding from the European Union's Horizon 2020 research and innovation program under the Marie Skłodowska-Curie grant agreement No 764513. Research was partially performed as part of the Center of Advanced Imaging Innovation and Research (CAI2R, www.cai2r.net), an NIBIB Biomedical Technology Resource Center (NIH P41 EB017183) and was partially supported by the NINDS (R01 NS088040) and NIBIB (R01 EB027075) of the NIH. The work was also supported by the Research Foundation Flanders (FWO Belgium) through project funding (G084217N and 12M3119N). The authors gratefully acknowledge support of the European Space Agency and BELSPO Prodex (BrainDTI).

Appendix. Computation of the CRLB matrix and derived metrics

In Eq. (14), $\boldsymbol{y}$ represents a set of N magnitude diffusion-weighted images, $\boldsymbol{\theta}$ the model parameter vector of size N_{par} and $p(\boldsymbol{y}|\boldsymbol{\theta})$ the joint probability density function (PDF) of $\boldsymbol{y}$ given $\boldsymbol{\theta}$. The CRLB matrix was derived assuming Gaussian distributed data, which is a valid approximation of the Rician distribution of the magnitude MRI data for SNR values larger than 2 (Gudbjartsson and Patz, 1995). Given a model $A_i(\boldsymbol{\theta})$ with $i = 1, \ldots, N$ and N being the number of independent Gaussian distributed data with the same σ, the Fisher information matrix can be expressed as (van den Bos, 2007):

$$\boldsymbol{I}(\boldsymbol{\theta}) = \frac{1}{\sigma^2} \sum_{i=1}^{N} \frac{\partial A_i}{\partial \boldsymbol{\theta}} \frac{\partial A_i}{\partial \boldsymbol{\theta}^T}, \tag{A.1}$$

where the derivatives of A_i with respect to $\boldsymbol{\theta}$ depend on the model selected to represent the data. By inverting $\boldsymbol{I}(\boldsymbol{\theta})$ we obtain the CRLB matrix of size $N_{par} \times N_{par}$, from which the absolute correlation coefficients can be derived as:

$$\left| r_{ij} \right| = \left| \frac{C_{ij}}{\sqrt{C_{ii} C_{jj}}} \right|, \tag{A.2}$$

with C_{ij} the ij^{th} element of the CRLB matrix. Finally, the absolute coefficients of variation are extracted as:

$$\left| CoV_i \right| = \left| \frac{\sqrt{C_{ii}}}{\theta_i} \right|, \tag{A.3}$$

with θ_i the ground truth value of the i^{th} parameter. While the correlation coefficients provide information about the identifiability of the model parameters, differences in the coefficients of variation quantify differences in attainable precision. More precisely, a reduction of the coefficients of variation means that the model parameters can be estimated (or, identified) with higher precision.

Supplementary material

Supplementary material associated with this article can be found, in the online version, at doi:10.1016/j.neuroimage.2022.119219.

References

Bai, Y., Alexander, D.C., 2008. Model-based registration to correct for motion between acquisitions in diffusion MR imaging. In: 2008 5th IEEE International Symposium on Biomedical Imaging: From Nano to Macro. IEEE, pp. 947–950.

Basser, P.J., Mattiello, J., LeBihan, D., 1994. MR diffusion tensor spectroscopy and imaging. Biophys. J. 66 (1), 259–267. doi:10.1016/S0006-3495(94)80775-1.

Beaulieu, C., 2014. The biological basis of diffusion anisotropy. In: Diffusion MRI. Elsevier, pp. 155–183.

Bergamino, M., Walsh, R.R., Stokes, A.M., 2021. Free-water diffusion tensor imaging improves the accuracy and sensitivity of white matter analysis in Alzheimer's disease. Sci. Rep. 11 (1), 1–12. doi:10.1038/s41598-021-86505-7.

Bergmann, Ø., Henriques, R., Westin, C.-F., Pasternak, O., 2020. Fast and accurate initialization of the free-water imaging model parameters from multi-shell diffusion MRI. NMR Biomed. 33 (3), e4219. doi:10.1002/nbm.4219.

Bojorquez, J.Z., Bricq, S., Acquitter, C., Brunotte, F., Walker, P.M., Lalande, A., 2017. What are normal relaxation times of tissues at 3T? Magn. Reson. Imaging 35, 69–80. doi:10.1016/j.mri.2016.08.021.

Byrd, R.H., Gilbert, J.C., Nocedal, J., 2000. A trust region method based on interior point techniques for nonlinear programming. Math. Program. 89 (1), 149–185. doi:10.1007/PL00011391.

Byrd, R.H., Hribar, M.E., Nocedal, J., 1999. An interior point algorithm for large-scale nonlinear programming. SIAM J. Optim. 9 (4), 877–900. doi:10.1137/S1052623497325107.

Cheng, J.Y., Zhang, T., Alley, M.T., Uecker, M., Lustig, M., Pauly, J.M., Vasanawala, S.S., 2017. Comprehensive multi-dimensional MRI for the simultaneous assessment of cardiopulmonary anatomy and physiology. Sci. Rep. 7 (1), 1–15. doi:10.1038/s41598-017-04676-8.

Chuhutin, A., Hansen, B., Jespersen, S.N., 2017. Precision and accuracy of diffusion kurtosis estimation and the influence of b-value selection. NMR Biomed. 30 (11), e3777. doi:10.1002/nbm.3777.

Clark, C.A., Hedehus, M., Moseley, M.E., 2001. Diffusion time dependence of the apparent diffusion tensor in healthy human brain and white matter disease. Magn. Reson. Med. 45 (6), 1126–1129. doi:10.1002/mrm.1149.

Collier, Q., Veraart, J., den Dekker, A.J., Vanhevel, F., Parizel, P.M., Sijbers, J., 2017. Solving the free water elimination estimation problem by incorporating T2 relaxation properties. In: Proceedings of the 25th Annual Meeting of ISMRM, Honolulu, Hawaii, p. 1783.

Collier, Q., Veraart, J., Jeurissen, B., Vanhevel, F., Pullens, P., Parizel, P.M., den Dekker, A.J., Sijbers, J., 2018. Diffusion kurtosis imaging with free water elimination: a bayesian estimation approach. Magn. Reson. Med. 80 (2), 802–813. doi:10.1002/mrm.27075.

Einstein, A., 1905. Über die von der molekularkinetischen Theorie der Wärme geforderte Bewegung von in ruhenden Flüssigkeiten suspendierten Teilchen. Ann Phys 322, 549–560. doi:10.1002/andp.19053220806.

Farrher, E., Buschbeck, R., Choi, C.-H., Kuo, L.-W., Yun, S.-D., Grinberg, F., Shah, N.J., 2018. In vivo DTI-based free-water elimination with T2-weighting. In: Proceedings of the Joint Annual Meeting of ISMRM-ESMRMB, Paris, France, p. 1629.

Farrher, E., Grinberg, F., Kuo, L.-W., Cho, K.-H., Buschbeck, R.P., Chen, M.-J., Chiang, H.-H., Choi, C.-H., Shah, N.J., 2020. Dedicated diffusion phantoms for the investigation of free water elimination and mapping: insights into the influence of T2 relaxation properties. NMR Biomed. 33 (4), e4210. doi:10.1002/nbm.4210.

Fieremans, E., Burcaw, L.M., Lee, H.-H., Lemberskiy, G., Veraart, J., Novikov, D.S., 2016. In vivo observation and biophysical interpretation of time-dependent diffusion in human white matter. Neuroimage 129, 414–427. doi:10.1016/j.neuroimage.2016.01.018.

Fieremans, E., Jensen, J.H., Helpern, J.A., 2011. White matter characterization with diffusional kurtosis imaging. Neuroimage 58 (1), 177–188. doi:10.1016/j.neuroimage.2011.06.006.

Fischi-Gomez, E., Rafael-Patino, J., Pizzolato, M., Piredda, G.F., Hilbert, T., Kober, T., Canales-Rodriguez, E.J., Thiran, J.-P., 2021. Multi-compartment diffusion MRI, T2 relaxometry and myelin water imaging as neuroimaging descriptors for anomalous tissue detection. In: 2021 IEEE 18th International Symposium on Biomedical Imaging (ISBI). IEEE, pp. 307–311.

Golub, M., Henriques, R.N., Nunes, R.G., 2021. Free-water DTI estimates from single b-value data might seem plausible but must be interpreted with care. Magn. Reson. Med. 85 (5), 2537–2551. doi:10.1002/mrm.28599.

Gudbjartsson, H., Patz, S., 1995. The Rician distribution of noisy MRI data. Magn. Reson. Med. 34 (6), 910–914. doi:10.1002/mrm.1910340618.

Hoy, A.R., Koay, C.G., Kecskemeti, S.R., Alexander, A.L., 2014. Optimization of a free water elimination two-compartment model for diffusion tensor imaging. Neuroimage 103, 323–333. doi:10.1016/j.neuroimage.2014.09.053.

Hoy, A.R., Ly, M., Carlsson, C.M., Okonkwo, O.C., Zetterberg, H., Blennow, K., Sager, M.A., Asthana, S., Johnson, S.C., Alexander, A.L., et al., 2017. Microstructural white matter alterations in preclinical Alzheimer's disease detected using free water elimination diffusion tensor imaging. PLoS ONE 12 (3), e0173982. doi:10.1371/journal.pone.0173982.

Jensen, J.H., Helpern, J.A., 2010. MRI quantification of non-Gaussian water diffusion by kurtosis analysis. NMR Biomed. 23 (7), 698–710. doi:10.1002/nbm.1518.

Jensen, J.H., Helpern, J.A., Ramani, A., Lu, H., Kaczynski, K., 2005. Diffusional kurtosis imaging: the quantification of non-Gaussian water diffusion by means of magnetic resonance imaging. Magn. Reson. Med. 53 (6), 1432–1440. doi:10.1002/mrm.20508.

Jerome, N.P., d'Arcy, J.A., Feiweier, T., Koh, D.M., Leach, M.O., Collins, D.J., Orton, M.R., 2016. Extended T2-IVIM model for correction of TE dependence of pseudo-diffusion volume fraction in clinical diffusion-weighted magnetic resonance imaging. Phys. Med. Biol. 61 (24), N667. doi:10.1088/1361-6560/61/24/N667.

Jeurissen, B., Tournier, J.-D., Dhollander, T., Connelly, A., Sijbers, J., 2014. Multi-tissue constrained spherical deconvolution for improved analysis of multi-shell diffusion MRI data. Neuroimage 103, 411–426. doi:10.1016/j.neuroimage.2014.07.061.

Jones, D.K., Horsfield, M.A., Simmons, A., 1999. Optimal strategies for measuring diffusion in anisotropic systems by magnetic resonance imaging. Magn. Reson. Med. 42 (3), 515–525. doi:10.1002/(SICI)1522-2594(199909)42:3<515::AID-MRM14>3.0.CO;2-Q.

Kellner, E., Dhital, B., Kiselev, V.G., Reisert, M., 2016. Gibbs-ringing artifact removal based on local subvoxel-shifts. Magn. Reson. Med. 76 (5), 1574–1581. doi:10.1002/mrm.26054.

Kim, D., Doyle, E.K., Wisnowski, J.L., Kim, J.H., Haldar, J.P., 2017. Diffusion-relaxation correlation spectroscopic imaging: a multidimensional approach for probing microstructure. Magn. Reson. Med. 78 (6), 2236–2249. doi:10.1002/mrm.26629.

Lampinen, B., Szczepankiewicz, F., Mårtensson, J., van Westen, D., Hansson, O., Westin, C.-F., Nilsson, M., 2020. Towards unconstrained compartment modeling in white matter using diffusion-relaxation MRI with tensor-valued diffusion encoding. Magn. Reson. Med. 84 (3), 1605–1623. doi:10.1002/mrm.28216.

Lätt, J., Nilsson, M., Wirestam, R., Ståhlberg, F., Karlsson, N., Johansson, M., Sundgren, P.C., van Westen, D., 2013. Regional values of diffusional kurtosis estimates in the healthy brain. J. Magn. Reson. Imaging 37 (3), 610–618. doi:10.1002/jmri.23857.

Le Bihan, D., Mangin, J.-F., Poupon, C., Clark, C.A., Pappata, S., Molko, N., Chabriat, H., 2001. Diffusion tensor imaging: concepts and applications. J. Magn. Reson. Imaging 13 (4), 534–546. doi:10.1002/jmri.1076.

Le Bihan, D., Turner, R., Douek, P., 1993. Is water diffusion restricted in human brain white matter? An echo-planar NMR imaging study. Neuroreport 4 (7), 887–890. doi:10.1097/00001756-199307000-00012.

MATLAB, 2020. Version 9.9.0 (R2020b). The MathWorks Inc., Natick, Massachusetts.

Metzler-Baddeley, C., Jones, D.K., Belaroussi, B., Aggleton, J.P., O'Sullivan, M.J., 2011. Frontotemporal connections in episodic memory and aging: a diffusion MRI tractography study. J. Neurosci. 31 (37), 13236–13245. doi:10.1523/JNEUROSCI.2317-11.2011.

Metzler-Baddeley, C., O'Sullivan, M.J., Bells, S., Pasternak, O., Jones, D.K., 2012. How and how not to correct for CSF-contamination in diffusion MRI. Neuroimage 59 (2), 1394–1403. doi:10.1016/j.neuroimage.2011.08.043.

Nilsson, M., van Westen, D., Ståhlberg, F., Sundgren, P.C., Lätt, J., 2013. The role of tissue microstructure and water exchange in biophysical modelling of diffusion in white matter. Magn. Reson. Mater. Phys. Biol. Med. 26 (4), 345–370. doi:10.1007/s10334-013-0371-x.

Ould Ismail, A.A., Parker, D., Hernandez-Fernandez, M., Brem, S., Alexander, S., Pasternak, O., Caruyer, E., Verma, R., 2018. Characterizing peritumoral tissue using DTI-based free water elimination. In: International MICCAI Brainlesion Workshop. Springer, pp. 123–131.

Papadakis, N.G., Murrills, C.D., Hall, L.D., Huang, C.L.-H., Carpenter, T.A., 2000. Minimal gradient encoding for robust estimation of diffusion anisotropy. Magn. Reson. Imaging 18 (6), 671–679. doi:10.1016/s0730-725x(00)00151-x.

Parker, D., Ould Ismail, A.A., Wolf, R., Brem, S., Alexander, S., Hodges, W., Pasternak, O., Caruyer, E., Verma, R., 2020. Freewater estimatoR using iNtErpolated iniTialization (FERNET): Characterizing peritumoral edema using clinically feasible diffusion MRI data. PLoS ONE 15 (5), e0233645. doi:10.1371/journal.pone.0233645.

Pasternak, O., Maier-Hein, K., Baumgartner, C., Shenton, M.E., Rathi, Y., Westin, C.-F., 2014. The estimation of free-water corrected diffusion tensors. In: Westin, C.-F., Vilanova, A., Burgeth, B. (Eds.), Visualization and processing of tensors and higher order descriptors for multi-valued data. Springer, pp. 249–270.

Pasternak, O., Sochen, N., Gur, Y., Intrator, N., Assaf, Y., 2009. Free water elimination and mapping from diffusion MRI. Magn. Reson. Med. 62 (3), 717–730. doi:10.1002/mrm.22055.

Pasternak, O., Westin, C.-F., Bouix, S., Seidman, L.J., Goldstein, J.M., Woo, T.-U.W., Petryshen, T.L., Mesholam-Gately, R.I., McCarley, R.W., Kikinis, R., et al., 2012. Excessive extracellular volume reveals a neurodegenerative pattern in schizophrenia onset. J. Neurosci. 32 (48), 17365–17372. doi:10.1523/JNEUROSCI.2904-12.2012.

Piechnik, S.K., Evans, J., Bary, L.H., Wise, R.G., Jezzard, P., 2009. Functional changes in CSF volume estimated using measurement of water T2 relaxation. Magn. Reson. Med. 61 (3), 579–586. doi:10.1002/mrm.21897.

Pierpaoli, C., Jones, D.K., 2004. Removing CSF contamination in brain DT-MRIs by using a two-compartment tensor model. In: Proceedings of the 12th Annual Meeting of ISMRM, Kyoto, Japan, p. 1215.

Poot, D.H., den Dekker, A.J., Achten, E., Verhoye, M., Sijbers, J., 2010. Optimal experimental design for diffusion kurtosis imaging. IEEE Trans. Med. Imaging 29 (3), 819–829. doi:10.1109/TMI.2009.2037915.

Qin, Q., 2011. A simple approach for three-dimensional mapping of baseline cerebrospinal fluid volume fraction. Magn. Reson. Med. 65 (2), 385–391. doi:10.1002/mrm.22705.

Sasson, E., Doniger, G.M., Pasternak, O., Tarrasch, R., Assaf, Y., 2013. White matter correlates of cognitive domains in normal aging with diffusion tensor imaging. Front. Neurosci. 7, 32. doi:10.3389/fnins.2013.00032.

Slator, P.J., Palombo, M., Miller, K.L., Westin, C.-F., Laun, F., Kim, D., Haldar, J.P., Benjamini, D., Lemberskiy, G., de Almeida Martins, J.P., et al., 2021. Combined diffusion-relaxometry microstructure imaging: current status and future prospects. Magn. Reson. Med. doi:10.1002/mrm.28963.

Stanisz, G.J., Odrobina, E.E., Pun, J., Escaravage, M., Graham, S.J., Bronskill, M.J., Henkelman, R.M., 2005. T1, T2 relaxation and magnetization transfer in tissue at 3T. Magn. Reson. Med. 54 (3), 507–512. doi:10.1002/mrm.20605.

Stejskal, E.O., Tanner, J.E., 1965. Spin diffusion measurements: spin echoes in the presence of a time-dependent field gradient. J. Chem. Phys. 42 (1), 288–292. doi:10.1063/1.1695690.

Tabesh, A., Jensen, J.H., Ardekani, B.A., Helpern, J.A., 2011. Estimation of tensors and tensor-derived measures in diffusional kurtosis imaging. Magn. Reson. Med. 65 (3), 823–836. doi:10.1002/mrm.22655.

Tax, C.M.W., Kleban, E., Chamberland, M., Baraković, M., Rudrapatna, U., Jones, D.K., 2021. Measuring compartmental T2-orientational dependence in human brain white matter using a tiltable RF coil and diffusion-T2 correlation MRI. Neuroimage 236, 117967. doi:10.1016/j.neuroimage.2021.117967.

Topgaard, D., 2017. Multidimensional diffusion MRI. J. Magn. Reson. 275, 98–113. doi:10.1016/j.jmr.2016.12.007.

Tournier, J.-D., Smith, R., Raffelt, D., Tabbara, R., Dhollander, T., Pietsch, M., Christiaens, D., Jeurissen, B., Yeh, C.-H., Connelly, A., 2019. MRtrix3: a fast, flexible and open software framework for medical image processing and visualisation. Neuroimage 202, 116137. doi:10.1016/j.neuroimage.2019.116137.

van den Bos, A., 2007. Parameter Estimation for Scientists and Engineers. John Wiley & Sons.

Veraart, J., Novikov, D.S., Christiaens, D., Ades-Aron, B., Sijbers, J., Fieremans, E., 2016. Denoising of diffusion MRI using random matrix theory. Neuroimage 142, 394–406. doi:10.1016/j.neuroimage.2016.08.016.

Veraart, J., Novikov, D.S., Fieremans, E., 2018. TE dependent diffusion imaging (TEdDI) distinguishes between compartmental T2 relaxation times. Neuroimage 182, 360–369. doi:10.1016/j.neuroimage.2017.09.030.

Veraart, J., Van Hecke, W., Sijbers, J., 2011. Constrained maximum likelihood estimation of the diffusion kurtosis tensor using a Rician noise model. Magn. Reson. Med. 66 (3), 678–686. doi:10.1002/mrm.22835.

Waltz, R.A., Morales, J.L., Nocedal, J., Orban, D., 2006. An interior algorithm for nonlinear optimization that combines line search and trust region steps. Math. Program. 107 (3), 391–408. doi:10.1007/s10107-004-0560-5.

Wang, S., Peng, Y., Medved, M., Yousuf, A.N., Ivancevic, M.K., Karademir, I., Jiang, Y., Antic, T., Sammet, S., Oto, A., et al., 2014. Hybrid multidimensional T2 and diffusion-weighted MRI for prostate cancer detection. J. Magn. Reson. Imaging 39 (4), 781–788. doi:10.1002/jmri.24212.

Whittall, K.P., Mackay, A.L., Graeb, D.A., Nugent, R.A., Li, D.K.B., Paty, D.W., 1997. In vivo measurement of T2 distributions and water contents in normal human brain. Magn. Reson. Med. 37 (1), 34–43. doi:10.1002/mrm.1910370107.